Article:

Moore, J, Beinlich, A, Piazolo, S orcid.org/0000-0001-7723-8170 et al. (2 more authors) (2020) Metamorphic Differentiation via Enhanced Dissolution along High Permeability Zones. Journal of Petrology, 61 (10). egaa096. ISSN 0022-3530

https://doi.org/10.1093/petrology/egaa096

Metamorphic Differentiation via Enhanced Dissolution along High Permeability Zones

Journal:	*Journal of Petrology*
Manuscript ID	JPET-Jun-20-0083.R1
Manuscript Type:	Original Manuscript
Date Submitted by the Author:	13-Sep-2020
Complete List of Authors:	Moore, Jo; The Institute for Geoscience Research, Curtin University, School of Earth and Planetary Sciences Beinlich, Andreas; The Institute for Geoscience Research, Curtin University, School of Earth and Planetary Sciences; University of Bergen, Department of Earth Science Piazolo, Sandra ; University of Leeds, Austrheim, Håkon; Physics of Geological Processes, University of Oslo Putnis, Andrew; Curtin University, The Institute for Geoscience Research; University of Münster, Institut für Mineralogie
Keyword:	Amphibolite facies, dissolution precipitation, mass transfer, metamorphic differentiation, thermodynamic modelling

Metamorphic Differentiation via Enhanced Dissolution along High Permeability Zones

Jo Moore[1]*, Andreas Beinlich[1, 2], Sandra Piazolo[3], Håkon Austrheim[4], Andrew Putnis[1, 5]

[1]The Institute for Geoscience Research (TIGeR), School of Earth and Planetary Sciences, Curtin University, Perth, WA, 6845, Australia

[2]Department of Earth Science, University of Bergen, Allégaten 41, 5007 Bergen, Norway

[3]School of Earth and Environment, University of Leeds, Leeds, UK

[4]Physics of Geological Processes (PGP), The Njord Centre, Department of Geosciences, University of Oslo, 0316, Oslo, Norway

[5]Institut für Mineralogie, University of Münster, 48149 Münster, Germany

** Corresponding author (Tel: +61403560643 E-mail: josephine.moore@postgrad.curtin.edu.au)*

ABSTRACT

Metamorphic differentiation, resulting in segregated mineral bands, is commonly recorded in metamorphic rocks. Despite the ubiquitous nature of compositionally layered metamorphic rocks, the processes that are responsible for metamorphic differentiation receive very little attention. Here, detailed petrography, quantitative mineral chemistry and bulk rock analyses are applied to investigate compositional variations and assemblage microstructure. Furthermore, thermodynamic modelling is applied to provide additional constraints on the P–T–X_{H2O} conditions of assemblage formation and mass transfer. The studied outcrop, located within the Bergen arcs of southwestern Norway, preserves the hydration of anorthositic granulite at amphibolite-facies conditions. The amphibolite-facies hydration is expressed as both a statically hydrated amphibolite and a shear zone lithology, defined by the interlayering of amphibolite with leucocratic domains. Within the granulite, quartz-lined fractures surrounded by amphibolite-facies alteration haloes represent relics of initial fluid infiltration associated with brittle failure. The fracture assemblage (quartz + plagioclase + zoisite + kyanite ± muscovite ± biotite) is identical to that occurring within leucocratic domains of the shear zone. Consequently, the compositional layering of the shear zone lithology is linked to fluid infiltration along localised zones of high permeability that result from fracturing. Mass-balance calculations indicate that quartz-lined fractures and compositional differentiation of the shear zone resulted from mass redistribution internal to the shear zone rather than partial melting or precipitation of minerals from externally derived fluid. The process of internal fractionation within the shear zone is driven by enhanced dissolution along highly permeable fracture planes resulting in the loss of MgO, Fe^{tot} and K_2O from the leucocratic domains. Elements dissolved in the fluid are then transported and ultimately either precipitated in comparatively impermeable amphibolite domains or removed from the system resulting in an overall mass loss. The mass transfer causing metamorphic differentiation of the shear zone is the result of coupled reaction and diffusion under differential stress. The mechanisms of mass redistribution observed within this shear zone provides further insight into the processes that facilitate mass transfer in the Earth’s crust.

Key words

Amphibolite facies; dissolution precipitation; mass transfer; metamorphic differentiation; thermodynamic modelling

INTRODUCTION

Fluid-driven mass transfer is a vital component of the processes that facilitate the chemical differentiation of the Earth's crust, the formation of mineral deposits and local lithospheric weakening. Mass transfer may be recorded at many scales in metamorphic rocks. At large scales, mass transfer may be responsible for volume losses during regional metamorphism (see e.g. Ague, 1994) and ductile shearing (see e.g. Dipple & Ferry, 1992, Selverstone *et al.*, 1991) as well as volume increase in extensional settings, generally expressed by the formation of veins or dykes. At the mm-cm scale, mass transfer is expressed by formation of local mineral assemblages and compositional banding, and at the grain-scale it may be observed as compositional zoning in minerals (Putnis & Austrheim, 2013). Understanding the processes responsible for compositional banding in metamorphic rocks, often referred to as metamorphic differentiation (Williams, 1972, 1990), is important as the processes driving and facilitating diffusional mass transfer are likely independent of the scale of the system. A better understanding of the driving forces behind metamorphic differentiation should therefore provide better insight to mass transfer processes in the crust as a whole.

The processes that facilitate metamorphic differentiation have been discussed extensively in the framework of experimental studies and observations of metasedimentary sequences (Dipple *et al.*, 1990, Fisher, 1970, Vernon, 1979, Vernon, 1998, Williams, 1990, Wintsch *et al.*, 1991, Wintsch & Andrews, 1988). While a general consensus on the exact mechanisms behind metamorphic differentiation has not been met, two broad requirements are consistent amongst most contributions; an imposing differential stress (Dewers & Ortoleva, 1990) and transport along a chemical potential gradient (Bons & Jessell, 1997, Dipple *et al.*, 1990, Fisher, 1970, Joesten, 1977). In most metamorphic environments, reactions occurring due to mm-cm scale chemical potential gradients will be reliant on the presence of a grain boundary fluid phase (Fisher, 1970, Rutter, 1983). Experimental evidence indicates that the rate of intergranular solid-state diffusion is sluggish in comparison to diffusion through an intergranular fluid medium (Carlson, 2010, Rubie, 1986, Yund, 1997). By comparison, the intergranular diffusion of elements through grain boundary fluid – commonly referred to as either pressure solution or dissolution-precipitation creep – occurs at significantly faster rates (Oelkers & Helgeson, 1988) potentially inducing large-scale rock transformations on short timescales (Beinlich *et al.*, 2020). Hence, diffusion through interconnected grain boundary fluid will enable significant mass transport through the crust wherever the rock is sufficiently saturated with fluid and may link areas of incompatible equilibrium conditions, i.e. drive mass transport along a chemical potential gradient.

Earlier studies on metamorphic differentiation via mass transfer were focused on the exchange of elements between adjacent sedimentary layers, and thus the chemical potential gradient could be attributed to the incompatibility of the original compositional layering during metamorphism (e.g. Orville, 1969, Vidale, 1969, Williams, 1972). In the cases where mass transfer has effected a relatively homogenous protolith and/or mass transfer is occurring on a scale larger than that defined by compositional layering, the driving force responsible for creating the chemical potential gradient is inferred to be either directly or indirectly the result of the imposed differential stress during metamorphism. In studies where the chemical potential gradient is inferred to be a direct result of differential stress, local equilibrium conditions may be created by the translation of the heterogeneous stress field to local thermodynamic pressures (Dahlen, 1992, Wheeler, 2014, 2018). Consequently, high pressure metamorphic assemblages would form where the normal stress is at a maximum. Indirectly, differential stress has been theorised to induce chemical potential gradients by affecting reaction kinetics. For example, dissolution is inferred to be enhanced at high stress boundaries while precipitation will be enhanced at low stress sites due to the creation of cavities (Rutter, 1976). The local reaction that occurs will be dependent on the rate-controlling step, whether that be dissolution, precipitation or mass transport, the rate-controlling step should differ depending on the local conditions. If, within the same rock, local zones of opposing reaction kinetics are connected by a grain boundary fluid then this is likely to result in a local chemical potential gradient. This has been demonstrated to occur during diagenesis, during which heterogeneous permeability distributions under conditions favourable for dissolution-precipitation-driven reaction result in the formation of a compositionally banded rock (Kelka *et al.*, 2017). While earlier work has primarily addressed the processes driving the mass transfer and the resulting metamorphic differentiation and volume loss in metasedimentary rocks, the same fundamental processes should be applicable to all metamorphic rocks.

Here we present a detailed analysis of the amphibolite-facies hydration of relatively homogenous anorthositic granulite of the Bergen arcs, southwestern Norway. In the outcrop, texturally uniform statically hydrated amphibolite-facies rocks sharply transition into a compositionally layered rock in a shear zone, providing an ideal locality to investigate the processes behind fluid and strain-facilitated mass transfer and metamorphic differentiation. Comparison of textural observations and chemical distribution amongst these lithologies suggest that dissolution is enhanced in zones of relatively high permeability, producing chemical potential gradients that then drive mass transfer.

GENERAL GEOLOGICAL BACKGROUND

The Bergen arcs constitute the hanging wall of the extensional Bergen arc shear zone. It is defined as a set of nappes, including the focus of this study, the Lindås Nappe (Fig. 1a). The Lindås Nappe mainly consists of an anorthosite-mangerite-charnockite-granite (AMCG) suite and banded gneiss complexes. Following intrusion pulses between 1237 +45/-35 Ma to 945 ± 33 Ma (Austrheim, 1990, Bingen *et al.*, 2001), the magmatic suite has undergone pervasive recrystallization at granulite facies conditions. The timing of the granulite facies recrystallization is constrained between 929 Ma (Bingen *et al.*, 2001) and 910 ± 10 Ma (Cohen *et al.*, 1988). Subsequently, Caledonian (~460-400 Ma) metamorphism along fluid conduits resulted in the localized transformation of the Lindås Nappe granulite to either amphibolite or eclogite, the latter of which is restricted to the westernmost extension of the nappe on the island of Holsnøy (Austrheim, 1987, Bingen *et al.*, 2001, Boundy *et al.*, 1996, Glodny *et al.*, 2002, 2008, Moore *et al.*, 2020).

The study outcrop is located on Radøy and preserves a Caledonian granulite to amphibolite reaction interface. Here, amphibolite-facies alteration has been constrained to ambient conditions of ~590-730°C and 10-14 kbar, based on thermodynamic modelling of the hydration of the granulite along grain boundaries (Moore *et al.*, 2019), Zr-in-rutile thermometry, and Al-in-hornblende barometry (Moore *et al.*, 2020). These P–T estimates are consistent with previous estimates of 690°C and 10–12 kbar (Boundy *et al.*, 1996), obtained using cation exchange thermobarometry in petrographically similar amphibolites of the Bergen arcs.

At the hydration interface, the amphibolite-facies assemblage inherits the overall texture of the granulite (Fig. 1c). As the amphibolite-facies rock becomes highly strained within the shear zone, it grades into compositionally distinct light and dark bands (Fig. 1b and e), allowing for a detailed investigation of the interplay between strain, inferred stress and mass transfer.

DESCRIPTION OF OUTCROP LITHOLOGIES

Three main rock types are present in the outcrop at Fjellsende; granulite, amphibolite, and the shear zone lithology consisting of a spaced foliation defined by bands of amphibolite and leucocratic feldspar-rich domains (Fig. 1b-e). The granulite away from the shear zone is characterised as a foliated, lilac coloured, and corona-bearing medium grained rock. In the granulite, the foliation is defined by the alignment of 1- 2 cm elongate, mafic clusters, consisting of diopside with garnet rims (Fig. 1c and d). At the granulite-amphibolite interface, hydration occurs via static replacement, evidenced by the continuity of the granulite foliation into the amphibolite (Fig. 1c). The amphibolite foliation, defined by elongate 1-2 cm clusters of amphibole, bends sharply within 50 cm of the shear zone boundary (Fig. 1b), thus forming a "strained" amphibolite. The foliation in the strained amphibolite is characterised by spaced 1-3 mm wide discontinuous amphibole-rich lenses surrounded by feldspar-rich domains. Within the strained amphibolite, foliation-parallel 1 cm wide bands of creamy pinkish feldspar and quartz appear at ~10 cm intervals. The shear zone lithology is characterized by the interlayering of dark and leucocratic bands (Fig. 1e). Dark bands are defined by a mixture of amphibole and feldspar, consistent with the mineralogy of the amphibolite. The leucocratic domains, which appear as creamy white bands, are mainly composed of feldspar with strongly aligned clinozoisite.

In addition to the three main rock types, veins and fractures are also observed. Pinkish 1 - 2 cm thick veins in the granulite are composed of scapolite and continue as brown-black discontinuous lenses, consisting of scapolite and amphibole, across the hydration interface into the amphibolite. Fractures are only clearly observed within the granulite and occur as sub-parallel stringers, striking approximately NW-SE (Fig. 1d). Haloes around quartz-lined fractures are composed of milky feldspar and coronas that have been partially replaced by amphibole.

METHODS

Sample preparation

For the granulite, amphibolite and the shear zone lithologies, thin section blocks and epoxy mounts were prepared parallel to the lineation (X direction) and normal to the foliation (XZ plane). Sections were carbon coated for scanning electron microscopy (SEM) and mineral chemical analysis.

Petrography and imaging

Microstructure was characterised with a standard petrographic microscope using plane-polarized light (PPL) and cross-polarized light (XPL). Backscattered electron (BSE) imaging was performed on the TESCAN MIRA variable pressure field emission scanning electron microscope (FE-SEM) at the John de Laeter Centre (JdLC), Curtin University, Perth, Australia. Imaging was performed with a beam energy of 25 kV at a working distance of 15 mm.

Quantification of phase abundance

Eight polished thin sections and 3 epoxy mounts were analysed using the TESCAN Integrated Mineral Analyser (TIMA3) FE-SEM at the JdLC, Curtin University, Perth, Australia. Analyses were performed using 4 PulseTor 30 energy dispersive X-ray (EDX) detectors at a working distance of 15 mm using a beam energy of 25 kV. Two modes of mapping were used: 7 thin sections underwent dot mapping at a 3 μm pixel size; 3 mounts and 1 thin section underwent and high-resolution mapping at a 5 μm pixel size. Phase maps were produced from output BSE and elemental X-ray maps using parameterised X-ray intensity brackets based on the chemistry of the known phases. Modal compositions have been calculated as an average phase area fraction of two to three thin sections or mounts for each of the main lithologies.

Quantitative analysis of mineral compositions

BSE imaging and quantitative geochemical analyses using energy dispersive spectroscopy (EDS) of minerals have been carried out on the TESCAN VEGA3 SEM at the Centre for Microscopy, Characterisation and Analysis (CMCA), The University of Western Australia. Analyses were performed at a working distance of 15 mm, an accelerating voltage of 15 kV and a beam intensity of 16 nA were used. All geochemical analyses were calibrated to an external standard (copper) and major element concentrations were determined to be accurate within ±2 wt%.

Additional quantitative geochemical point analyses and mapping using wavelength dispersive spectroscopy (WDS) were carried out on the JEOL JXA-8530F electron microprobe (EMPA) at the CMCA. All analyses were performed using an accelerating voltage of 15 kV, a beam current of 20 nA and spot size of 5 μm.

Amphibole and mica compositions were acquired using the following analysing crystals: TAP for Si Kα, Al Kα, Na Kα, and Mg Kα; PETJ for Ca Kα, Cl Kα and K Kα; LiF for Mn Kα and Fe Kα; and LiFH for Ti Kα and Cr Kα. Counting time was 30 s for all elements. Scapolite point analyses and element distribution maps were acquired using the following analysing crystals: TAP for Si Kα, Al Kα, Na Kα, and Mg Kα; PETJ for Ca Kα and K Kα; LiF for Ti Kα and Fe Kα; and PETH for S Kα, Cl Kα and P Kα. For these analyses the counting time was 20 s for all elements. The standards employed were commercially available silicates, oxides, and metals. Mean atomic number background corrections were employed throughout (Donovan & Tingle, 1996). Unknown and standard intensities were corrected for dead time and the ZAF algorithm was used for matrix absorption (Armstrong, 1988). On-peak interference corrections were applied as appropriate (Donovan *et al.*, 1992). Detection limits ranged from 60 ppm for Cl to 370 ppm for FeO.

Weight percent oxide data were recalculated into cations per formula unit for individual minerals, using 6 oxygens for diopside, 12 oxygens for garnet, 8 oxygens for plagioclase, 24 oxygens for scapolite, 23 oxygens for amphibole, 12.5 oxygens for clinozoisite and zoisite, and 11 oxygens for biotite. Amphibole was classified according to the scheme proposed by Hawthorne *et al.* (2012) using the spreadsheet of Locock (2014). In general, the calculation of and presentation of scapolite compositional data follows Porter and Austrheim (2017). The meionite component of scapolite was calculated using: 100 × Ca/ (Ca + Na). The equivalent anorthite component of scapolite was calculated using: 100 × (Al - 3)/ 3. The amount of C in scapolite was calculated using: $C_A = 1 – S_A – Cl_A$.

Whole rock chemical analysis

Eight samples underwent density measurements by weighing fist-sized specimen in air and water prior to whole rock analysis at Bureau Veritas Minerals Pty Ltd, Perth, Australia. Samples were crushed and then pulverised in a vibrating disc pulveriser. SiO_2, TiO_2, Al_2O_3, Fe_2O_3, MgO, CaO, Na_2O, K_2O, SO_3, Cu and Cl contents were determined by X-ray fluorescence (XRF) spectrometry on oven dry samples. Loss on ignition (LOI) was determined by heating the oven dry (105 °C) sample material to 1000 °C using a robotic thermogravimetric analyser (RTGA). FeO was determined volumetrically. Carbon was determined by total combustion analysis. The pulverised samples were cast u

sing a 66:34 flux with 4% $LiNO_3$ added to form a glass bead. Fused beads were analysed by Laser Ablation Inductively Coupled Plasma Mass Spectrometry (LA-ICP-MS) for trace and rare earth element concentrations of Ti, La, Ce, Pr, Nd, Sm, Eu, Gd, Tb, Dy, Ho, Er, Tm, Yb and Lu.

The granulite, amphibolite and strained amphibolite compositions represent an average of 2 analyses from separate samples, whereas the compositions of the amphibolite and leucocratic domains of the shear zone are based on 1 analysis each. The indicated error represents the combined sample variability and analytical uncertainty where more than 1 sample has been measured. Where only one sample has been analysed, the error reflects the analytical uncertainty only. The H_2O concentration is calculated from the LOI minus measured C (as CO_2) and SO_3. All Fe is considered as Fe_2O_3, noted as Fe^{tot}, for evaluation of its relative concentration changes.

Shear zone lithology composition

Due to the relatively wide spacing of compositionally distinct layers, the bulk composition of the shear zone was obtained by re-integrating the compositions of individual layers instead of analysing an unrealistically large sample. This was achieved through a combination of whole rock geochemistry and image analysis. Four separate images of the shear zone outcrop were analysed using Image-J (Rasband, 1997-2014) to quantify the proportion of dark to light components using standard thresholding. The separate amphibolite and leucocratic domain whole rock chemical analyses were then combined based on the calculated average proportions of 54±3% amphibolite and 46±3% leucocratic domains.

Thermodynamic modelling

Thermodynamic modelling was undertaken using the software THERMOCALC 3.45 (Powell & Holland, 1988) and the 'metabasite set' of activity-composition (a-X) models (Green *et al.*, 2016 and references therein), calibrated for use with version 6 of the dataset of Holland and Powell (2011). Solution models used are clinoamphibole (*hb*; Green et al., 2016), clinopyroxene (*dio, o*; Green et al., 2016), epidote (ep; Holland & Powell, 2011), garnet (g; White *et al.*, 2014), muscovite (*mu*; White et al., 2014), biotite (*bi*; White et al., 2014), ternary feldspar (pl; Holland

& Powell, 2003), and tonalitic 'metabasite' melt (*L*; Green et al., 2016). Mineral abbreviations follow solution models where applicable; elsewhere mineral abbreviations follow Whitney and Evans (2010).

The NCKFMASHTO (Na_2O-CaO-K_2O-FeO-MgO-Al_2O_3-SiO_2-H_2O-TiO_2-Fe_2O_3) system was used for all thermodynamic models. Uncertainty related to the absolute positions of assemblage field boundaries in any individual phase diagram is around ±0.1 GPa and ±50 °C at the 2σ level (Powell & Holland, 2008; Palin et al., 2016), although relative uncertainty is lower when comparing equilibria calculated using the same a–X relations and dataset. Here, individual P and T conditions are relatively precise to around ±0.02 GPa and ±10 °C (Worley & Powell, 2000). Additional uncertainty is expected due to the model system not considering Mn, which is known to expand the stability of garnet-bearing assemblages in metapelitic rock compositions (White *et al.*, 2014). As there are currently no Mn solution models for metabasic rocks, it is unclear whether Mn would have the same effect on the modelled garnet stability fields. Based on metapelitic model systems and the relatively low concentration of MnO in the studied rocks (~0.05%; Table 1), expansion of the garnet stability field towards lower pressure may be in the order of 0.1 GPa. Conversely, no effect on the temperature of garnet stability is expected (White *et al.*, 2014).

T–X_{H2O} modelling of the amphibolite composition was undertaken to obtain constraints on the amount of water present at equilibrium conditions. The observed amphibolite assemblage was not stable at the measured bulk rock H_2O content (0.26 wt%), indicating that the amount of water present during rock equilibration was not the same as the amount now mineralogically bound, suggesting that excess water was lost during the exhumation. Stability of the amphibolite mineral assemblage, using 3 modal% zoisite (see results), is obtained by a relative H_2O content increase of 110-135% (0.77-0.91 wt%). A 120% increase in H_2O was used for P–T modelling of the amphibolite (0.84 wt%) as this gave the best consistency with the P–T conditions provided by previous estimates. This procedure was repeated for the amphibolite and leucocratic domains of the shear zone lithology and the results are used for the calculation of P–T and P–X pseudosections for the relative lithologies.

RESULTS

General description of lithologies

In the following, representative samples of the main lithologies are described according to their mineralogical assemblage and microstructural features. In general, minerals can be divided into two categories (1) medium-grained (500 μm – 5 mm) anhedral, equi-granular grains in the granulite, and, (2) fine-grained minerals (< 500 μm) in the amphibolite and leucocratic domains as well as along grain boundaries and fractures in the granulite. For ease of description in the later sections, granulite that has undergone significant alteration (i.e. when the rock contains less than 30% clear feldspar: Fig. 2c) but still preserves relic pyroxene and garnet and an overall granoblastic texture is referred to as altered granulite.

Granulite

Although partially altered, the granulite preserves more than 80% clear feldspar in outcrop (Figs 1c, d and 2a) and is the closest representation of the precursor lithology. The assemblage comprises plagioclase (An_{58}) (70%), garnet (17%), diopside (9%), and scapolite (2%). Within the plagioclase dominated matrix, diopside grains form elongated clusters decorated by irregular coronas of garnet. Fine-grained amphibolite-facies minerals occurring along grain boundaries account for less than 2% of the rock. Grain boundary phases include amphibole, clinozoisite, zoisite, kyanite, biotite, chlorite, plagioclase, K-feldspar, muscovite, and quartz.

Altered granulite

The altered granulite is characterised by a greater extent of fine-grained minerals present as inclusions within the granulitic plagioclase (An_{58}) and at diopside, garnet and plagioclase grain boundaries (Fig. 2c). The assemblage comprises plagioclase (An > 40) (69%), garnet (13%), diopside (9%), and scapolite (2%). Fine-grained minerals occurring along grain boundaries form the same assemblage as in the granulite, however, here they constitute 7% of the rock (Fig. 2c; Fig. 3).

In both the granulite and the altered granulite, the spatial distribution of fine-grained (< 50 μm in diameter) amphibolite-facies minerals is highly dependent on the chemistry of the granulite host mineral (Figs. 2a-c and 4a, b). Diopside is replaced by a fine-grained assemblage of Mg-hornblende, quartz, clinozoisite, and rutile, whereas garnet is replaced by pargasite, kyanite and plagioclase. Primary plagioclase (An_{58}) is replaced by secondary plagioclase (An_{68-82}) with inclusions of zoisite, kyanite, and quartz.

Amphibolite

The amphibolite is defined by the complete disappearance of garnet and pyroxene and is composed of less than 30% clear feldspar (Fig. 1c). This lithology consists of a fine-grained assemblage of plagioclase (An > 40) (47%), amphibole (43%), zoisite (3%), kyanite (2%), and biotite (1%) with minor amounts (< 1% each) of clinozoisite, quartz, carbonate, scapolite, biotite, quartz, pyrite, and rutile (Figs 2d and 3). This assemblage is present as two domains: (1) plagioclase and (2) amphibole domains. Plagioclase domains (1) form the matrix of the rock and consist of plagioclase that is partially recrystallized to finer grained aggregates containing abundant zoisite, kyanite, and quartz inclusions. In addition to the abundant inclusions, plagioclase in the amphibolite displays reverse zoning, exhibiting relative An-depletion (An_{41-54}) in the inclusion free cores and An-enrichment (An_{64-88}) around inclusions and at grain rims.

Amphibole domains (2) form discontinuous small (1-2 mm) augen-shaped lenses to larger (5-10 mm wide) discontinuous lenses. Amphibole domains are more variable in composition. The compositional variability in amphibole domains is a consequence of the clustering of secondary phases according to the distribution of the pre-existing phases (Fig. 4c). Within these domains, clusters of fine-grained (20 – 200 μm) Mg-hornblende, quartz, carbonate, rutile, and pyrite mimic the geometry of the diopside (Fig. 2a-d). Similarly, the garnet replacement assemblage, as described for the altered granulite, consists of pargasite, kyanite and plagioclase with the addition of biotite (Fig. 4c).

Strained amphibolite

The strained amphibolite occurs within the zone of parallel fabric bordering the shear zone (Fig. 1b). It consists of plagioclase (An > 40) (59%), amphibole (18%), zoisite (8%), clinozoisite (3%), quartz (3%), kyanite (2%), chlorite (2%), scapolite (2%) muscovite (1%), and minor amounts (< 1% each) of biotite and rutile (Fig. 2e and 3). The increased quartz component in this lithology is attributed to the presence of foliation sub-parallel quartz domains. Outside of the quartz domains, four separate compositional domains can be distinguished within the strained amphibolite: (1) plagioclase-pure domains (Fig. 2e(i)), (2) plagioclase-zoisite domains (Fig, 2e(ii)), (3) amphibole domains (Fig. 2e(iii)) and (iv) plagioclase-amphibole domains (Fig. 2e(iv)).

Plagioclase-pure domains (1) are of similar composition to the plagioclase domains in the amphibolite, consisting primarily of recrystallized plagioclase with minor amounts of zoisite, kyanite and quartz. Comparatively, plagioclase-zoisite domains (2) contain an increased abundance and larger laths of zoisite and kyanite. Amphibole domains (3) consist of almost pure amphibole with minor amounts of quartz, zoisite, clinozoisite and biotite. Plagioclase-amphibole domains (4) are unique to the strained amphibolite and consist of a dispersed distribution of plagioclase, zoisite and amphibole.

Shear zone lithology

The shear zone lithology exhibits divisible compositional banding defined by the cm-scale interlayering of leucocratic domains with amphibolite. Within the leucocratic domains, quartz domains are also observed as discrete foliation-parallel bands.

The amphibolite domain within the shear zone consists of plagioclase (59%), amphibole (27%), clinozoisite (4%), zoisite (3%), kyanite (2%), scapolite (2%), and minor amounts (1% each) of quartz, biotite, muscovite, rutile, and chlorite (Figs. 2f and 3). The amphibolite domain can be further divided into subdomains: (1) plagioclase and (2) amphibole subdomains. These two subdomains compositionally resemble the plagioclase and amphibole domains of the amphibolite (Fig. 2d), however, the bands of amphibole in the shear zone form much more elongate sigmoidal lenses (Fig. 2f).

Leucocratic domains consist of plagioclase (74%), zoisite (6%), amphibole (5%), scapolite (5%), clinozoisite (4%), biotite (2%), and minor amounts (< 1% each) of quartz, kyanite, chlorite, muscovite, and rutile (Figs 2g and 3). The mineralogy and microstructure of these domains are largely consistent with the plagioclase-zoisite domains of the strained amphibolite (Fig. 2e(ii)) but with the addition of foliation-parallel stringers of quartz, biotite, clinozoisite, and muscovite (Fig. 2g(i)). Within the stringers rare highly elongate amphiboles may be observed (Fig. 2g(ii) and 4e).

Quartz-rich domains within the shear zone lithology occur exclusively within leucocratic domains. The quartz-rich domains consist of plagioclase (53%), zoisite (29%), quartz (9%), kyanite (3%), scapolite (3%), clinozoisite (1%), and minor amounts (< 1% each) of biotite, muscovite and rutile (Fig. 2h and 3).

Local quartz enrichment

Localised quartz enrichment occurs in the granulite, altered granulite, the strained amphibolite and within leucocratic domains of the shear zone (Figs 2 and 5). In the least altered granulite, local quartz enrichment occurs along fractures (Figs. 1d and 2b). The fractures are lined by a 200-600 μm wide assemblage of quartz, albite-oligoclase, bytownite and biotite (Figs. 2b(i) and 5a). Quartz along the fracture forms aggregates of 50 to 150 μm grains with planar-curved quartz-quartz and quartz-albite-oligoclase grain boundaries, commonly meeting at 120° triple junctions (Fig. 5b). Smaller (5 to 50 μm) quartz and albite-oligoclase grains and quartz grain aggregates are dispersed within a network of fine-grained (10 to 20 μm) bytownite and biotite. Quartz and albite-oligoclase grain boundaries in contact with this fine-grained network are deeply embayed.

The alteration haloes of these fractures are evidenced by extensive replacement of the host plagioclase by an assemblage consisting of zoisite, quartz, and kyanite ± muscovite (Fig. 5a). Zoisite, quartz and kyanite all occur as 5-20 μm anhedral grains dispersed within plagioclase. However, with increasing proximity to the fractures, zoisite becomes more angular and lath-like. Zoisite forms grains up to 1 mm in length closest to the fracture. Where the alteration halo dissects diopside and garnet, the assemblage consists predominantly of amphibole, with minor plagioclase, clinozoisite, zoisite, and biotite (Fig. 2b(i)).

Additional quartz-lined fractures are observed within the altered granulite (Fig. 5c). The assemblage within these fractures comprises quartz, oligoclase, bytownite, scapolite, and tschermakite ± calcite. Quartz-quartz boundaries are curved-planar, commonly meeting at 120° triple junctions. Additionally, quartz shares planar to gently curved boundaries with oligoclase, scapolite, and tschermakite. Tschermakite forms tabular well-faceted to slightly rounded grains with 50 to 150 μm in diameter. Quartz grain boundaries are also embayed when in contact with bytownite, but to a lesser degree compared to grain boundaries with albite-oligoclase.

A 2-3 mm wide foliation sub-parallel quartz domain is observed within the strained amphibolite (Fig. 5d). This layer has a distinct mineralogy in comparison to the surrounding amphibolite (Fig. 2e). Quartz occurs as foliation-parallel aggregates of 100 to 200 μm grains and as dispersed 20 to 50 μm cuspate grains (Fig. 5d and e) in a matrix of muscovite, biotite, and oligoclase. Muscovite exhibits sharp and irregular K- and Mg-poor rims (Fig. 5e), associated with a bright phase, most likely either zircon, rutile, or pyrite, that is apparent along grain boundaries and in interstitial voids. An-rich plagioclase (labradorite-bytownite) occurs as rims around oligoclase and is evident at quartz grain boundaries, associated with embayment of the quartz grain boundary. Associated with the quartz-enriched domain in the strained amphibolite are 150 to 400 μm long, foliation-parallel laths of zoisite and clinozoisite and kyanite grains with 100 to 200 μm in diameter (Fig. 2e and 5d).

Foliation sub-parallel quartz domains of 3 -5 mm in width are also observed within leucocratic domains in the shear zone (Fig. 2h and 5f). Here, quartz appears as 100 to 200 μm grains forming foliation-parallel aggregates as well as dispersed 10 to 100 μm sized grains.

Dispersed quartz grains occur as an interstitial phase within foliation-parallel clusters of zoisite and globular 20 to 50 μm sized kyanite grains. An-poor plagioclase (andesine) rimmed by a relatively An-rich plagioclase (labradorite) hosts the interstitial quartz, zoisite, and kyanite (Fig. 5f).

Amphibole and scapolite mineral chemistry

Amphibole and scapolite mineral compositions associated with the various lithologies have been analysed to determine and characterise compositional changes across lithological and structural transitions; in particular, to trace variations in volatile concentration involved in the amphibolite-facies alteration and to determine the changes in amphibole composition associated with the decreased amphibole abundance in the shear zone. Representative amphibolite and scapolite mineral compositions are reported in Electronic Appendix 1.

Amphibole

In all analysed amphibole mineral recalculations, Ca is entirely hosted within the B-site. The Ca-amphibole plot has been modified accordingly to indicate that A-site occupancy is represented entirely by Na and K (Fig. 6a). For all measured amphibole compositions, an increase in Cl concentration is coupled with a decrease in X_{Mg} and an increase in A-site occupancy (Fig. 6a and b). The most Cl-enriched amphibole (0.02 atoms per formula unit (apfu)) exhibits an X_{Mg} of 0.56 and A-site occupancy of 0.58 and the least Cl-enriched (Cl below detection limit) exhibits an X_{Mg} of 0.81 and A-site occupancy of 0.06 (Fig. 6a and b).

Amphibole at grain boundaries in the least altered granulite occurs as Mg-hornblende and pargasite (Fig. 6a). Pargasitic amphibole is hosted at diopside-plagioclase and garnet-plagioclase grain boundaries (Fig 4a). Mg-hornblende occurs within symplectites of quartz, clinozoisite, and rutile, replacing diopside or as cores within pargasitic grains. Within the granulite amphibole, X_{Mg} ranges between 0.73-0.85 and Cl concentration is less than 0.002 apfu.

Amphibole in the altered granulite varies in composition (Fig. 6a). Pargasite is the most common composition, occurring in the diopside replacement assemblage as well along fractures in the plagioclase (Fig. 5c). In association with fractures, Mg-hornblende may appear as cores within pargasitic grains. Tschermakite and sandanagaite predominantly occur at garnet rims (Fig. 4b). Within the altered granulite, Cl concentration varies (0.001-0.018 apfu, X_{Mg} 0.57-0.79) and the highest concentration of Cl in amphibole occurs in fractures (0.018 apfu, X_{Mg}=0.57).

In the amphibolite, the amphibole composition is predominantly Mg-hornblende (Fig. 6a); particularly for smaller (50-100 μm) grains that occur within the diopside replacement assemblage (e.g. Fig 4c). Pargasite and sandanagaite are larger (more than 100 μm) and occur either as part of the garnet replacement assemblage or at the boundaries between amphibole clusters and plagioclase (Fig. 4c). Chlorine concentration in the amphibole in the amphibolite is consistently low, ranging between 0.002 and 0.006 apfu (X_{Mg} 0.63-0.72) (Fig. 6b).

In the strained amphibolite, the amphibole composition is comparatively constant and classifies as Mg-hornblende (Fig. 6a). The Cl concentration varies between 0.001 and 0.009 Cl apfu with X_{Mg} 0.62-0.78 (Fig. 6b).

The composition of amphibole varies within the shear zone. In leucocratic domains, where amphibole occurs as highly elongate grains embayed by muscovite and quartz (Fig. 4e), the composition is dominantly Mg-hornblende (Fig. 6a). These highly elongate amphibole grains are texturally associated with the alteration of muscovite to biotite (Fig. 4e). Exhibiting a similar composition to amphibole in the strained amphibolite, amphibole in the leucocratic domains has a lower Cl concentration (0.003-0.006 Cl apfu) and exhibits a slightly decreased X_{Mg} (0.56-0.69)

(Fig. 6b). In the amphibolite domains, amphibole occurs in clusters with quartz, clinozoisite, zoisite, biotite, and rutile (Fig. 4d). The composition of amphibole in the amphibolite domains varies between Mg-hornblende, tschermakite, sandanagaite, and pargasite (Fig. 6a). Furthermore, it has the most consistently increased Cl concentration between 0.002-0.02 Cl apfu and the lowest X_{Mg} values (0.53-0.70).

Scapolite

Scapolite is present in all lithologies. In the granulite, scapolite occurs as 150 μm to 5 mm sized granoblastic grains, either as clusters dispersed throughout the plagioclase matrix or as discrete veins (Fig. 7c). The chemical composition of scapolite is reported according to the normalised components of S, Cl, and C in the A-site, the meionite component (X_{Me}) and an equivalent anorthite component (EqAn; see methods for details on calculation) (Fig. 7a and b). The larger granoblastic grains in the altered granulite exhibit a consistent core composition with an average EqAn of 0.62, X_{Me} of 0.73 and A-site occupancy of $S_{0.72}C_{0.28}$. The composition of scapolite in the least altered granulite was not measured, however, the consistency between these core compositions and those reported Porter and Austrheim (2017) from nearby granulitic scapolite veins (EqAn of 0.49-0.54, X_{Me} of 0.61-0.64 and A-site occupancy of $S_{0.68\text{-}0.69}C_{0.24\text{-}0.25}$; for location see Fig. 1a) suggest that the cores preserved in the altered granulite are close to original granulitic composition. At rims of large grains and around zoisite inclusions, the EqAn (0.61) and X_{Me} (0.72) components are not significantly different. However, the A-site occupancy becomes slightly more C-enriched with a composition of $S_{0.63}C_{0.36}Cl_{0.01}$ (Fig. 7a (i)). Small grains (< 60 μm in diameter) occur at the boundaries of large scapolite grains and along fractures (Fig. 7d). Small grains present at granulitic scapolite grain boundaries have a consistent EqAn component of 0.57 and X_{Me} of 0.57. In contrast, the A-site occupancy is highly variable $S_{0.09\text{-}}$

$_{0.62}C_{0.37-0.89}Cl_{0.01-0.02}$ (Fig. 7a (ii)). Small grains in fractures have a comparatively consistent C and Cl-rich composition of $S_{0.10}C_{0.87}Cl_{0.04}$ and slight Na-enrichment with an EqAn of 0.48 and X_{Me} of 0.58 (Fig. 7a: fracture).

In the amphibolite, scapolite forms aggregates of similar shape and size to the precursor granulitic scapolite (Fig. 7e). However, the A-site occupancy of $S_{0.03-0.16}C_{0.83-0.96}Cl_{0.01-0.02}$ is relatively C-rich. The EqAn component is 0.53-0.58 and X_{Me} is 0.66-0.71, only slightly lower than that of the granulitic scapolite.

Scapolite in the strained amphibolite and the shear zone lithology are similar in composition (Fig. 7a and b). The EqAn component of scapolite in the strained amphibolite ranges from 0.55-0.62 and X_{Me} ranges between 0.64-0.68, while the A-site occupancy shows a variation of $S_{0.21-0.42}C_{0.57-0.78}Cl_{0.01-0.02}$. Scapolite in the shear zone lithology is more variable in composition with an EqAn component that varies from 0.49-0.57, X_{Me} between 0.60-0.69, and the A-site occupancy of $S_{0.06-0.43}C_{0.56-0.91}Cl_{0.01-0.03}$.

Mass balance across fracture alteration haloes

Mass transfer associated with fractures and their alteration haloes were assessed using quantitative major element maps of the granulitic plagioclase, the fracture alteration halo, and the fracture assemblage in the granulitic plagioclase. The integrated average compositions of each of the map areas are compared to quantify whether the amphibolite-facies hydration is associated with an influx of (non-volatile) major elements. Maps and the total composition of the map areas are given in Electronic Appendix 2a and b, respectively.

For the map areas only SiO_2, Al_2O_3, CaO, Na_2O, and K_2O were present in concentrations above the detection limit. All detectable element oxide concentrations overlap within the uncertainty and are consistent with stoichiometric plagioclase. SiO_2 and Al_2O_3 make up the major component of the map areas at 53.9 wt% and 30.0 wt% in the granulitic plagioclase, 53.9 wt% and 29.8 wt% in the alteration halo, and 54.9 wt% and 29.9 wt% in the fracture. CaO, Na_2O, and K_2O can be simplified as relative proportions of An and Or-components in the map area. Neither the fracture ($An_{56}Or_2$) nor the alteration halo ($An_{57}Or_2$) exhibit a significant change in composition in comparison to the granulitic plagioclase ($An_{58}Or_2$).

Changes in whole rock composition related to hydration and deformation

Mass balance

The whole rock chemistry of the main amphibolite-facies lithologies amphibolite, amphibolite domains, the leucocratic domains, and the re-integrated shear zone lithology is presented in the form of mass change relative to the precursor granulite, based the constant mass reference frame (Grant, 1986). The strained amphibolite is excluded from the mass-balance calculation due to its compositional heterogeneity (e.g. Fig. 2e), which may result in an erroneous interpretation of mass change. Using the constant mass reference frame negates the need to define one or more immobile elements, hence eliminating the uncertainty involved with choosing the correct geochemical reference frame for a metasomatised system (Ague & Van Haren, 1996). The choice of using fixed mass is further verified by the only minor hydration-related density changes from 2.87 g/cm^3 in the granulite to 2.86 g/cm^3 in the amphibolite. The amphibolite domain has a density of 2.89 g/cm^3 and the leucocratic domain has a density of 2.80 g/cm^3. Whole rock compositions and densities are given in Table 1.

Major elements. Similar distributions are observed for Al_2O_3 and CaO, both showing only very minor mass change, decreasing in the amphibolite (-2% and -3%) and amphibolite domains (-4% and -2%), but increasing in the leucocratic domains (+10% and +5%) and the re-integrated shear zone lithology (+2% and +1%) (Fig. 8). SiO_2 and Na_2O are similarly coupled, increased in the leucocratic domains (+2% and +22%), decreased in the amphibolite (-1% and -2%) and the amphibolite domains (-4% and -10%) accounting to an overall loss of SiO_2 (-1%) and gain of Na_2O (+5%) in the re-integrated shear zone lithology. Mass gains of K_2O are exhibited in the amphibolite domains (+21%) and the re-integrated shear zone lithology (+9%), while losses are observed in the amphibolite (-12%) and the leucocratic domains (-6%). In comparison to the other major elements, Fe^{tot} and MgO show much greater mobility. An increase of Fe^{tot} concentration occurs in the amphibolite (+11%) and the amphibolite domains (+50%) but decreased concentrations occur in leucocratic domains (-75%) and the re-integrated shear zone lithology (-7%), relative to the granulite. Similarly, the MgO concentration is increased in the amphibolite (+16%) and amphibolite domains (+24%), but exhibits loss in the leucocratic domains (-87%) and the re-integrated shear zone lithology (-27%) (Fig. 8).

Volatile elements and Cl. Water is increased in all amphibolite-facies lithologies relative to the granulite (Fig. 8). The amphibolite and amphibolite domains exhibit the same relative increase in H_2O (both +280%). The leucocratic domains of the shear zone exhibit the highest concentration of H_2O, increased by +400%, producing a re-integrated shear zone lithology H_2O mass gain of +340%. Chlorine increases by over +3000% in amphibole-bearing lithologies, with the strongest increase observed in the amphibolite domains (+6200%; Fig. 8). In the leucocratic domain, Cl concentrations are 500% higher than in the granulite. The SO_3 concentration is uniformly increased across all amphibolite-facies lithologies, varying from +180% in the amphibolite domains to +190% in the amphibolite. In contrast, CO_3 only exhibits increased concentration in the amphibole-bearing rocks. The largest increase is observed in the amphibolite

(+100%), whereas the amphibolite domains exhibits only a small increase (+33%). The increase in CO_3 in the amphibolite domains seems balanced by a mass loss in the leucocratic domains (-33%), producing an overall mass change of +3% CO_3 in the re-integrated shear zone lithology.

Rare earth element patterns

Rare earth element (REE) concentrations are presented here normalised to chondrite (McDonough & Sun, 1995) (Fig. 9). The REE patterns are presented for the purpose of evaluating whether there is any significant REE fractionation across the hydration and deformation interface, due to either original compositional variation or mass transfer during metamorphism.

Changes in concentration of REE across the shear zone interface result in only very minor differences in patterns. All lithologies exhibit steeply dipping REE patterns with a marked Eu anomaly. The Eu anomalies for each lithology a broadly similar with the largest anomaly observed in the amphibolite (Eu/Eu* = 4.22) and the smallest in the amphibolite domains (Eu/Eu* = 2.48). The fractionation of REE is similar for the granulite ($La/Yb_N = 8.47$), the strained amphibolite ($La/Yb_N = 7.59$), and the amphibolite domains ($La/Yb_N = 8.92$). The amphibolite is slightly more fractionated ($La/Yb_N = 12.85$), owing to an apparent loss of medium to heavy REE relative to the granulite. By comparison, the leucocratic domains appear slightly more fractionated ($La/Yb_N = 20.3$) due to a significant increase of light REEs, without an increase in M-HREE, relative to the granulite.

P-T-X_{H2O} constraints on amphibolite formation and the shear zone

The amphibolite, the amphibolite domains and leucocratic domains have been modelled in T–X_{H2O} pseudosections (Fig. 10a-c) to constrain the amount of fluid present during equilibration of the observed assemblages. For each of the presented models, the X_{H2O} composition is the measured H_2O content at X_0 and a near 400% increase of molar% H_2O at X_1. Epidote composition is consistent with the observed composition ($X_{czo} > 0.95$) within all modelled conditions. Complete P–T pseudosections for each of the lithologies presented in Fig. 10 are provided in Electronic Appendix 3.

For both amphibolite assemblages, T–X_{H2O} modelling indicates an increased H_2O component during equilibration of the observed assemblage relative to the measured amount (Fig. 10a and b). In both the amphibolite and amphibolite domain T–X_{H2O} sections the stability of the garnet-absent mineral assemblage is tightly constrained by the garnet-producing reaction, occurring at predominantly lower T–X_{H2O} compositions. The H_2O component is constrained by zoisite modal isopleths at 3 modal% for both amphibolite lithologies (Fig. 3). For both lithologies, H_2O concentration estimates represent a range that is close to the maximum ambient temperature estimate of 730°C while remaining below the solidus. At temperatures between 675-720°C the amphibolite has an estimated 0.77-0.91 wt% H_2O and at temperatures between 670-715°C the amphibolite domain has an estimated 0.95-1.10 wt% H_2O. The median values of 0.84 wt% H_2O for the amphibolite and 1.03 wt% H_2O for the amphibolite domains have been taken to produce the mineral stability fields in P–T space (Fig. 10d). In contrast to the amphibolite assemblages, the leucocratic domain assemblage (6 modal% zoisite) is stable at the measured H_2O content (X_0; 0.48 wt%) at ~705°C (Fig. 10c). When modelled in P–T space, all lithologies produce mineral stability fields that are in agreement with previous estimates of 590-730°C and 1.0-1.4 GPa for the conditions of amphibolite-facies metamorphism that are derived from mineral thermobarometry (Fig. 10d) (see also Moore et al., 2020 and references therein). The stability of the assemblages of the individual lithologies overlap at peak conditions of 720°C and

1.14 GPa. At these conditions, the calculated water activities (α_{H2O}) for the Thermocalc reactions are 0.63 for the amphibolite, 0.77 for the amphibolite domains and 0.87 for the leucocratic domain assemblages.

Modelling of shear zone mineralogical distribution in P-X space

Based on the bulk H_2O content derived from the T–X_{H2O} pseudosection calculations, we evaluate in P–X space whether the mineral distribution in the shear zone is consistent with the attainment of thermodynamic equilibrium during or subsequent to mass transfer, and whether the segregation of the two distinct shear zone lithologies occurred at the same P–T conditions (Fig. 11a). The P–X pseudosection has been fixed at 720°C, consistent with the observed assemblage and Zr-in-rutile thermometry (Fig. 10d). This temperature represents an upper limit and was inferred to reflect near peak metamorphic conditions. For the P–X sections, X_0 represents the amphibolite domain composition and X_2 the leucocratic domain composition as in Fig. 10d and Electronic Appendix 3.

Additional mass-balance calculations, using constant mass as the reference frame, for the two shear zone lithologies relative to the re-integrated shear zone lithology and the re-integrated shear zone lithology relative to the granulite are presented within Fig, 11a, to enable comparison with partial melt calculations. The leucocratic and amphibolite domain compositions indicate a close to balanced exchange of Na_2O, H_2O, K_2O, Cl, Fe^{tot}, and MgO between the two lithologies (Fig. 11a). The amphibolite domain is relatively depleted in Na_2O (-14%) while exhibiting mass gains in H_2O (+33%), K_2O (+11%), Cl (+71%), Fe^{tot} (+62%), and MgO (+70%). In the leucocratic domains, the reciprocal trend is observed, here Na_2O is gained (+16%) while H_2O (-38%), K_2O (-13%), Cl (-84%), Fe^{tot} (-73%), and MgO (-82%) are relatively depleted. Discrepancies of more than 10% mass change of Fe^{tot} , MgO, and Cl between the leucocratic domain and the amphibolite domains are consistent with the observed total mass loss of Fe^{tot} (-7%) and MgO (-27%) and mass gain of Cl (+3600%) in the re-integrated shear zone lithology relative to the granulite composition (Fig. 8g and 11a). Furthermore, the depletion of MgO and Fe^{tot} in the leucocratic domains corresponds with the observed (X_0: 27%, X_2: 5%; Fig. 3 and 11c) and modelled (X_0: 39%, X_2: 4%; Fig. 11b) decreased modal abundance of amphibole.

As in the T–X_{H2O} pseudosection, equilibrium conditions for the amphibolite domains assemblage are also constrained in the P–X space by the garnet-in and the zoisite-out reactions to 1.09- 1.19 GPa (X_0; Fig. 11a). However, the zoisite modal abundance is only consistent with the observed value (3%; Fig. 3 and 11c) in the presence of partial melt (1%) in the assemblage (Figure 11a and b). If the pressure estimate is based on the zoisite 3% modal isopleth, the stability of the amphibolite domains assemblage is constrained to 1.10±0.04 GPa at X_0.

For the leucocratic domains, garnet is not stable at any of the presented P–T conditions (Fig. 10c and 11a). The stability of the mineral assemblage is instead confined by the muscovite-out reaction at 1.24 GPa and the zoisite-out reaction at 1.12 GPa. Also, for the leucocratic domains, the observed zoisite modal abundance (6%) can only be reproduced in the presence of partial melt (1%) (Fig. 11a and b). Based on the 6% modal isopleth for zoisite the stability of the assemblage in the leucocratic domains is constrained to 1.14±0.01 GPa at X_2.

Composition of partial melt approximated from thermodynamic modelling

P–X modelling indicates that partial melt may have been present during at least one stage of metamorphism of the shear zone lithology (Fig. 11a and c). The calculated melt composition is presented for comparison with the observed elemental mobility (Fig. 12 and Electronic Appendix 4). As this is an investigation of the composition that would result from hydration-induced melting, a T–X_{H2O} diagram has been constructed for the granulite (Electronic Appendix 3), and melt compositions have been calculated at 720°C and 11 kbar with 1, 5, and 9% melt component. Based on these estimates the expected mass changes in the solid residuum and the liquid relative to the anhydrous granulite have been calculated.

At the low degree of partial melting, the produced melt is primarily a hydrous aluminosilicate with a composition of ~62% SiO_2, ~16% Al_2O_3, and ~13% H_2O. In terms of mass change relative to the granulite precursor, melting involved mass gains in the melt component in Na_2O (9-20%), SiO_2 (23%), K_2O (670-900%), and H_2O (> 10,000%).

The main compositional change occurring during the partial melting is the fractionation of H_2O and K_2O into the melt, resulting in a 740-800% mass gain in H_2O and a 38-52% mass loss of K_2O in the residual solid (Fig. 12). At 1, 5, and 9% partial melt SiO_2, Na_2O, CaO and Al_2O_3 all exhibit <5% mass loss while FeO and MgO exhibit mass gains of 7-10 and 6-9%, respectively.

DISCUSSION

Quartz enrichment on fracture planes

Quartz-lined fractures in the granulite (Fig. 2c) and the quartz-enriched domains within the strained amphibolite and the leucocratic domains (Fig. 5) are mineralogically and texturally similar. They are associated with planar aligned clusters of quartz containing abundant zoisite laths (100 µm – 1mm), particularly in the alteration haloes. The main difference between quartz-lined fractures and quartz-enriched domains is that the latter are aligned as foliation-parallel bands (Fig. 2e, h and 5d, f). The mineralogical and textural resemblance of the quartz-lined fractures and quartz-enriched domains suggests a common origin of these features, with the foliation-parallel quartz-enriched domains having undergone further deformation during or after their formation.

Furthermore, the amphibolite mineral assemblage, comprising plagioclase, amphibole, zoisite, kyanite, clinozoisite, and quartz ± scapolite ± biotite (Fig. 2d), is consistent with that of the fracture alteration haloes in the granulite (Fig. 2c), suggesting that the fractures formed during initial fluid infiltration or represent pre-existing high permeability pathways that were later exploited by infiltrating fluids to produce the amphibolite assemblage. Within the shear zone lithologies, quartz-enriched domains are exclusively found within the leucocratic domains (Fig. 2). A quartz-enriched domain is also observed in the strained amphibolite, associated with a higher abundance of zoisite and plagioclase in comparison to the amphibolite (Figs. 2d, e and 3). The association between quartz-enriched domains and increased plagioclase and zoisite abundance suggests that they may be integral to understanding the processes driving the formation of leucocratic domains, and hence the differentiation of the shear zone lithology. The intimate interlayering of the leucocratic and the amphibolite domains in the shear zone lithology suggests that the quartz-enriched, leucocratic and amphibolite domains formed during the same metamorphic event. In addition, the observed replacement of amphibole by quartz and biotite within leucocratic domains (Fig. 4e) indicates that the processes driving the segregation of the rock into quartz-enriched domains, and by extrapolation, leucocratic and amphibolite domains, continued after the initial amphibolite-forming hydration event.

Externally derived elements vs. internal fractionation

To gain insight into the mechanism of metamorphic differentiation within the shear zone, the composition of the infiltrating fluid is examined to determine whether the observed compositional variation of the rock is the result of externally derived major element addition.

The whole rock analysis reveals mass gains in H_2O, SO_3, and Cl in all lithologies relative to the granulite (Fig. 8), indicating that the infiltrating fluid was not purely water. The whole rock mass gain of Cl in the amphibolite and shear zone lithologies is in agreement with the analysis of fluid inclusions from quartz veins from the nearby Holsnøy metamorphic complex (for location see Fig. 1a) (Andersen *et al.*, 1991). The authors report two types of veins, one occurring in the centre of amphibolite-facies shear zones and another one exhibits alteration haloes in statically hydrated granulite, i.e. similar to the occurrence of quartz at Fjellsende. Fluid inclusion compositions from the reported veins are between 2-50 wt% $NaCl_{eq}$ and molar $CaCl_2/(CaCl_2 + NaCl)$ ratios of 0.28 in the shear zone and 0-0.4 in the smaller veins in the granulite, indicating the presence of saline fluid during amphibolite-facies metamorphism. The Na and Ca contents of these fluid inclusions is at odds with the whole rock analysis of this study which indicates no significant mass gain or loss of those elements across the hydration interface (Fig. 8). Indeed, quantitative analysis of alteration haloes in plagioclase reveals that there was no significant gain or loss of plagioclase forming oxides (SiO_2, Al_2O_3, Na_2O, K_2O and CaO) associated with fracturing and fluid infiltration (Electronic Appendix 2). Other major elements (Fe^{tot}, MgO, and TiO_2) are below their detection limits and hence did not undergo measurable mass gain (Electronic Appendix 2). Given the lack of evidence for significant influx of externally derived Na, Ca, and Si, the reported elevated Na and Ca contents in fluid inclusions (Andersen et al., 1991) is deemed to be most likely the result of local fluid-rock reactions instead of being characteristic of amphibolitization fluids at a larger scale. Consequently, it is inferred that quartz-lined fractures associated with the amphibolite-facies event cannot be formed as the result of precipitation of major element oxides from an infiltrating fluid, and are instead formed as a result of the internal fractionation and recrystallization of the host rock during the infiltration of a Cl-bearing aqueous fluid.

The absence of mass gain is consistent further with the whole rock mass-balance calculation for the re-integrated shear zone lithology, indicating insignificant major element gains relative to the granulite (Fig. 8d). There is, however, a considerate loss of MgO in the shear zone (-27%; Fig. 8d), particularly from the leucocratic domains (Fig. 8c and 11a). This depletion of MgO is evidenced not only by the mass balance but also by the observed breakdown of amphibole within these domains (Fig. 4e). The highly elongate nature of the grains and the protruding neighbouring quartz and mica are indicative of incongruent dissolution of the amphibole (Wassmann & Stöckhert, 2013). Furthermore, the associated sharp irregular zones of biotite replacing muscovite indicate mass transport during the breakdown reaction. Even though these reactions may be expected during the partial melting of a rock undergoing differential stress, the modelled patterns of element redistribution via partial melting is inconsistent with the recorded mass change in the shear zone lithology (Fig. 12). Modelling of partial melting of the granulite indicates a melt component that should be relatively enriched in SiO_2, Na_2O, and K_2O and a solid residual component that would be relatively depleted of feldspar forming elements and enriched in FeO and MgO. Consequently, the redistribution of elements in the shear zone lithology was by fluid–rock interaction that was also accompanied but not driven-by partial melting.

Reaction mechanism

We infer that dissolution-precipitation is the governing reaction mechanism. This interpretation is corroborated by textural evidence, including sharp reaction fronts in partially replaced plagioclase (Fig. 4b and 5c), diopside (Fig. 4a), and garnet (Fig. 4a and c) in the granulite, as well as sharp and irregular compositional fronts in muscovite (Fig. 4e and 5e) and plagioclase (Fig. 5e) in the amphibolite assemblages (Putnis, 2009). While the thermodynamic modelling does not indicate that H_2O was in excess during the transformation of the granulite to amphibolite (Fig. 10a-c and Electronic Appendix 3) the a-X solution models are limited to pure H_2O fluid compositions and thus cannot preclude the presence of a more compositionally complex fluid. We argue that the textural evidence alone is sufficient to suggest the presence of free fluid during the amphibolite-facies metamorphism. Despite the relatively high temperature, mineral replacement driven by solid-state diffusional modification of phase compositions is generally slower than mineral replacement by dissolution-precipitation reactions mechanism (Pattison, 1994, Rubie, 1986), and thus solid-state mechanisms are unlikely to be dominant.

Interface-coupled dissolution-precipitation reactions involve three main processes; dissolution of precursor mineral at the interface, precipitation of reaction products, and diffusive transport to and from the reaction front (Rutter, 1983, Xia *et al.*, 2009). Whichever of the processes is the slowest is the rate-limiting step. The assemblages forming the statically hydrated amphibolite and the quartz-lined fractures exhibit contrasting reaction microstructures. In the amphibolite and at grain boundaries in the granulite, static replacement of anhydrous granulite-facies minerals by fine-grained aggregates of amphibolite-facies minerals is evident (Fig. 4a and b). Amphibolite-facies mineral assemblages maintaining morphological and chemical evidence of the phases they have replaced in the completely reacted amphibolite (Fig. 4c and d). When replacement of a mineral during a hydration reaction is pseudomorphic, as is observed in the amphibolite (Fig. 4c), then it is theorised that the replacement process is rate-limited by dissolution at the interface (Xia *et al.*, 2009). In contrast, when precipitation is rate-limiting then solute transport is likely to occur, resulting in mass loss at the dissolution interface.

Within the quartz-lined fractures and quartz-enriched domains, there is no evidence for the direct replacement of host minerals by the newly formed quartz (e.g. mineral inclusions). Furthermore, the clusters of quartz and plagioclase lining the fracture walls, and scapolite and tschermakite in the fractures exhibit characteristic curved-planar grain boundaries, commonly forming 120° triple junctions (Fig. 5). This microstructure is indicative of low interfacial energy and characteristic for grain growth from a free fluid (see Vernon, 2018). Consequently, precipitation must have been decoupled from dissolution, consistent with the presence of amphibole and biotite as fracture filling in plagioclase (Fig. 5a and c), requiring external MgO and Fe^{tot}. However, the length scale of mass transport must have been shorter than resolvable at the given sampling resolution (Fig. 8).

In addition to textural evidence for the decoupling of precipitation from dissolution, we also observe distinct chemical compositions of minerals between the statically hydrated amphibolite and fracture fillings (Fig. 6 and Fig. 7a and b). For example, within the same thin section, both amphibole and scapolite in fractures in the altered granulite exhibit higher Cl concentrations in comparison to grains formed by replacement of diopside and garnet in the static amphibolite. Given the systematic relationship between Cl concentration and microstructure and considering the predominantly aqueous composition of the fluid, it is unlikely that the difference in Cl concentration results from compositional heterogeneity in the infiltrating fluid. The observed higher fluid inclusion salinity (20-50 wt% $NaCl_{eq}$) in quartz-lined fractures in statically hydrated granulite compared with shear zones (2-16 wt% $NaCl_{eq}$) (Andersen *et al.*, 1991), are more consistent with closed system (mm-cm scale fluid connectivity; Fig. 13d), rock-buffered conditions where H_2O-consuming hydration reactions increase fluid salinity in the fractures (see also Lamadrid *et al.*, 2017, Markl & Bucher, 1998, Markl *et al.*, 1998).

Conversely, the shear zone represents a relatively open system (> cm scale fluid connectivity; Fig. 13e) allowing for fluid-buffered mineral growth.

Given the previous work on fluid inclusions of Andersen *et al.* (1991), it can be argued that for the thermodynamically modelled lithologies (Fig. 10) the calculated water activity can be used as a proxy for salinity, as a decreased water activity would be expected where salinity is increased. The calculated water activity for the equilibrium assemblages was lowest in the amphibolite ($\alpha H_2O = 0.63$), higher in the amphibolite domains ($\alpha H_2O = 0.77$) and highest in the leucocratic domains ($\alpha H_2O = 0.87$) (Fig. 10d). These values are consistent with the measured higher salinity of fluid inclusions within the statically hydrated alteration haloes in comparison to the shear zone (see above discussion), further supporting the interpretation that formation of the leucocratic domains was via aqueous fluid-buffered reactions, in comparison to those occurring during the static hydration of the amphibolite.

The partitioning of Cl into amphibole and scapolite appears to be more effective in fractures (Fig. 6 and 7) and increased amphibole Cl concentrations are also observed in the amphibolite domains in comparison to the statically hydrated amphibolite (Fig. 6). The observation of increased Cl content in amphibole texturally associated with more deformed, plagioclase-rich lithologies has been described previously (Kullerud, 1996). This author attributes the Cl enrichment in amphiboles to growth from an evolved, rock-buffered fluid in a closed system. This model is consistent with that described above for the increased salinity of fluid inclusions associated with fractures in the granulite and may also explain the increased Cl content of scapolite and amphibole in fractures (Fig. 6 and 7).

Dissolution-precipitation driven mass transfer

Two types of reaction zones can be broadly defined for the amphibolite-facies hydration event; those in which the reaction rate is limited by dissolution (i.e. the amphibolite and the amphibolite domains), and those where precipitation is the rate-limiting step thus enhancing mass transport (i.e. quartz-lined fractures and leucocratic domains). The formation and evolution of these reaction zones is illustrated schematically in Fig. 13.

Quartz-enriched domains are texturally and compositionally analogous to quartz-lined fractures, with the exception that, despite being strained, quartz-enriched domains occupy wider zones (3-5 mm) in comparison to quartz-lined fractures (200-600 μm; Fig. 2b and h). Quartz-enriched domains are thus interpreted as larger versions of quartz-lined fractures, representing a snapshot of the initial amphibolite-facies fluid infiltration (Fig. 13a). After the initial fracturing, the fractures and their damage zones form zones of relatively high permeability. These high permeability zones are of two-fold importance for the distribution of dissolution and precipitation reactions: they allow the influx and mobility of fluid within the unaltered granulite, instigating the amphibolite-facies reactions, and, they allow for locally decreased pore-fluid pressure.

In the following section a coupling between the increased permeability around fractures and the reaction mechanism is theorised. For simplicity and consistency with the referenced literature, the following discussion will refer to stress using only normal stress, neglecting the shear stress component. The relevance and intricacies of the application of shear stresses in systems undergoing reaction, maintained by a grain boundary fluid, have been discussed more thoroughly in previous contributions and are beyond the scope of this work (for review see; Wheeler, 2018).

Decreased pore-fluid pressure is essential for maintaining differential stresses during reaction. This is most easily demonstrated by the following equation:

(1) $\sigma_{eff} = \sigma_n - P_f$

where σ_{eff} is the effective normal stress, σ_n is the normal stress and P_f is the interconnected pore fluid pressure (Cox, 2010, Hill, 2015). It follows that as P_f approaches the value of σ_n than σ_{eff} will be reduced and the tensile strength of the rock may be exceeded, resulting in brittle failure (Cox, 2010). The maintenance of low pore-fluid pressure is therefore necessary for continued reaction at high differential stresses. Continued low pore-fluid pressure may be achieved where high permeability is maintained along zones where the initial damage, fluid infiltration, and reaction were significant enough to produce weakening and ultimately deformation (Fig. 13b and e). Conversely, where the reacting volume is closed off to further fluid/mass exchange (Fig. 13d), the volume increase associated with the hydration reactions (Centrella *et al.*, 2015) will both work to further seal the rock from fluid replenishment and increase the pore-fluid pressure so that the effective normal stress is subdued.

Two endmembers for the conditions under which reactions proceed can be established; (I; Fig. 13d) where, following initial fluid infiltration, reactions proceed in a closed system under relatively low differential stress coinciding with dissolution-limited reaction (i.e. the amphibolite and amphibolite domains) and (II; Fig. 13e) where continued permeability allows for high differential stresses to be maintained, coinciding with precipitation-limited reaction (i.e. quartz-lined fractures and leucocratic domains). Based on these scenarios it then follows that there are two possible key factors that influence the difference in reaction products between each of these scenarios; (1) the contrasting length-scales of elemental mobility and (2) the relative permeability of the rock during reaction.

The length-scale of mass transport (1) or interconnected porosity is important as it controls the bulk composition of the equilibrium system and thus determines the products of the reaction. This can be demonstrated using Figure 11a as an example. Assuming a rock with bulk composition X_0 is chemically isolated (i.e. closed system) and equilibrates at 1.2 GPa then the resulting mineral assemblage will be: hornblende, garnet, plagioclase, clinozoisite, muscovite, quartz, kyanite, and zoisite. If that rock is, however, connected via a fluid saturated network of pores with an equivalent mass of rock with bulk composition X_2 then the equilibrium composition will now be approximately X_1 and the equilibrium assemblage at 1.2 GPa will no longer contain garnet. This relies on the assumption that element diffusion is primarily facilitated by the grain boundary fluid and that minerals are in local equilibrium with the grain boundary fluid. Both are reasonable assumptions given that mineral replacement proceeds as dissolution-precipitation reaction and that fluid is in excess. Differing length-scales of element mobility can explain the local occurrence of extreme compositions, inherited from the original compositional variation of the rock (i.e. where transport length-scales are small; Fig. 13d). Accordingly, at larger mass transport length-scales, there should be a homogenisation of the compositional heterogeneity that results from the original mineral distribution. Hence, while fluid connectivity will facilitate element exchange, a gradient caused by a disparity in either the rates or driving force of reaction between the compositionally distinct layers is further required for differentiation.

Here, the interpretation is based on the observation of distinct zones exhibiting (I) reaction under conditions where permeability, effective normal stress, and dissolution are decreased vs. (II) reaction under conditions where permeability, effective normal stress, and dissolution are increased. The inference being that the relative permeability and hence the effective normal stress influences the rate of dissolution. Increased dissolution in areas of increased effective normal stress is consistent with the proposition that stress enhances dissolution via increasing the elastic energy through deformation of a grain surface (Den Brok *et al.*, 2002, Den Brok & Morel, 2001, Koehn *et al.*, 2003). Furthermore, it commonly asserted that increased stress on an interface will result in a relatively increased chemical potential at that interface (Paterson, 1973, Shimizu, 1995, Wheeler, 2018). Areas of high effective normal stress will then have a strong chemical potential relative to relatively low stress areas (Rutter, 1983, Wintsch, 1985). The resulting chemical potential gradient enables mass transport towards low permeability zones where precipitation will take place. Correlation between high permeability, stress and enhanced dissolution has been observed and modelled elsewhere for systems undergoing reaction via dissolution and precipitation (Kelka *et al.*, 2017), producing a compositionally and texturally banded rock via mass exchange.

Enhanced dissolution in localised high-permeability areas coupled with distinct element solubilities and preferential mobilization of MgO, K_2O, and Fe^{tot} may thus explain the presence of quartz-enriched and leucocratic domains. Leucocratic domains may then form as zones of strain-enhanced dissolution (Fig. 13b) around quartz-enriched domains, resulting in the mobilization of MgO, K_2O, and Fe^{tot} by a dilute NaCl-bearing aqueous fluid (Fig. 13e). The relative depletion of K_2O, Fe^{tot}, and MgO and minor enrichment of SiO_2, Al_2O_3, Na_2O, and CaO in the leucocratic domains are consistent with previous experimental work indicating that Si and Al are far less mobile in Cl-bearing fluids than metals (Shmulovich *et al.*, 2001, Vidale, 1969). The differences in element mobility can be related to distinct solubilities of Na, Ca, and Mg in saline fluid due to the formation of fluid-mobile alkali and earth-alkali Cl complexes (Anderson & Burnham, 1983, Shmulovich *et al.*, 2001). The mass-balance calculation indicates that the mobilized elements were then either transported and precipitated into amphibolite domains of the shear zone or mobilized from the system, resulting in the slight overall mass loss from the shear zone.

CONCLUSIONS

A common interpretation of quartz-enriched microstructures in amphibolite and eclogite-facies metamorphic environments is that they form via the precipitation of externally derived elements. Mass-balance calculations indicate that in this instance the quartz-enrichment observed along fractures and within the shear zone lithology is indicative of localised mass loss. Localised depletion of MgO, Fe^{tot} and K_2O around high dissolution seams is due to the increased compatibility of these elements with the infiltrating Cl-bearing aqueous fluid relative to the reacting solid. Locally enhanced dissolution thus provides an alternative mechanism for the localisation of elements in high-pressure environments.

Locally enhanced dissolution around fracture pathways ultimately results in the metamorphic differentiation of the shear zone lithology, and on a larger scale also to the observed differentiation of elements between the statically hydrated rock and the shear zone lithologies. The coupling between enhanced dissolution leading to mass loss along high permeability zones and the relative gain of elements in statically hydrated rocks supports dissolution-precipitation facilitated mass transfer. Mass transfer is driven by chemical potential and solubility gradients. Here it is demonstrated that deviations in permeability and hence effective normal stress may result in the formation of both chemical potential and solubility gradients.

ACKNOWLEDGEMENTS

This manuscript has been improved by the review of U. Kelka, R. Palin and one anonymous reviewer. An early version of this manuscript was reviewed by J. Ague and C. Spandler. This research was funded by the Australian Research Council Discovery Project of Putnis, Raimondo, and Daczko (ARC grant number DP160103449). The authors acknowledge the facilities, and the scientific and technical assistance of the Australian Microscopy and Microanalysis Research Facility at the Centre for Microscopy, Characterisation and Analysis, The University of Western Australia, a facility funded by the University, State and Commonwealth Governments. Part of this research was undertaken using the EM instrumentation (ARC LE130100053) at the John de Laeter Centre, Curtin University.

DATA AVAILABILITY

The data underlying this article are available in the article and in its online supplementary material.

REFERENCES

Ague, J. J. (1994). Mass transfer during Barrovian metamorphism of pelites, south-central Connecticut; I, Evidence for changes in composition and volume. *American Journal of Science* **294**, 989-1057.

Ague, J. J. & Van Haren, J. L. (1996). Assessing metasomatic mass and volume changes using the bootstrap, with application to deep crustal hydrothermal alteration of marble. *Economic geology* **91**, 1169-1182.

Andersen, T., Austrheim, H. & Burke, E. A. J. (1991). Fluid-induced retrogression of granulites in the Bergen Arcs, Caledonides of W. Norway: Fluid inclusion evidence from amphibolite-facies shear zones. *Lithos* **27**, 29-42.

Anderson, G. & Burnham, C. W. (1983). Feldspar solubility and the transport of aluminum under metamorphic conditions. *American Journal of Science* **283 A**, 283-297.

Armstrong, J. (1988). Quantitative analysis of silicate and oxide materials: comparison of monte carlo, ZAF, and ψ (ρz) procedures. *Microbeam analysis*, 239-246.

Austrheim, H. (1987). Eclogitization of lower crustal granulites by fluid migration through shear zones. *Earth and Planetary Science Letters* **81**, 221-232.

Austrheim, H. (1990). Fluid induced processes in the lower crust as evidenced by Caledonian eclogitization of Precambrian granulites, Bergen Arcs, western-Norway.

Beinlich, A., John, T., Vrijmoed, J., Tominaga, M., Magna, T. & Podladchikov, Y. (2020). Instantaneous rock transformations in the deep crust driven by reactive fluid flow. *Nature Geoscience* **13**, 307-311.

Bingen, B., Davis, W. J. & Austrheim, H. (2001). Zircon U-Pb geochronology in the Bergen arc eclogites and their Proterozoic protoliths, and implications for the pre-Scandian evolution of the Caledonides in western Norway. *Geological Society of America Bulletin* **113**, 640-649.

Bons, P. D. & Jessell, M. W. (1997). Experimental simulation of the formation of fibrous veins by localised dissolution-precipitation creep. *Mineralogical magazine* **61**, 53-63.

Boundy, T. M., Essene, E. J., Hall, C. M., Austrheim, H. & Halliday, A. (1996). Rapid exhumation of lower crust during continent-continent collision and late extension: Evidence from ^{40}Ar/^{39}Ar incremental heating of hornblendes and muscovites, Caledonian orogen, western Norway. *Geological Society of America Bulletin* **108**, 1425-1437.

Boundy, T. M., Mezger, K. & Essene, E. J. (1997). Temporal and tectonic evolution of the granulite-eclogite association from the Bergen Arcs, western Norway. *Lithos* **39**, 159-178.

Carlson, W. (2010). Dependence of reaction kinetics on H2O activity as inferred from rates of intergranular diffusion of aluminium. *Journal of Metamorphic Geology* **28**, 735-752.

Centrella, S., Austrheim, H. & Putnis, A. (2015). Coupled mass transfer through a fluid phase and volume preservation during the hydration of granulite: An example from the Bergen Arcs, Norway. *Lithos* **236**, 245-255.

Cohen, A., O'nions, R., Siegenthaler, R. & Griffin, W. (1988). Chronology of the pressure-temperature history recorded by a granulite terrain. *Contributions to Mineralogy and Petrology* **98**, 303-311.

Cox, S. (2010). The application of failure mode diagrams for exploring the roles of fluid pressure and stress states in controlling styles of fracture-controlled permeability enhancement in faults and shear zones. *Geofluids* **10**, 217-233.

Dahlen, F. (1992). Metamorphism of nonhydrostatically stressed rocks. *American Journal of Science* **292**, 184-198.

Den Brok, B., Morel, J. & Zahid, M. (2002). In situ experimental study of roughness development at a stressed solid/fluid interface. *Geological Society, London, Special Publications* **200**, 73-83.

Den Brok, S. & Morel, J. (2001). The effect of elastic strain on the microstructure of free surfaces of stressed minerals in contact with an aqueous solution. *Geophysical Research Letters* **28**, 603-606.

Dewers, T. & Ortoleva, P. (1990). Geochemical self-organization III: A mechano-chemical model of metamorphic differentiation. *Am. J. Sci* **290**, 473-521.

Dipple, G., Wintsch, R. & Andrews, M. (1990). Identification of the scales of differential element mobility in a ductile fault zone. *Journal of Metamorphic Geology* **8**, 645-661.

Dipple, G. M. & Ferry, J. M. (1992). Metasomatism and fluid flow in ductile fault zones. *Contributions to Mineralogy and Petrology* **112**, 149-164.

Donovan, J. J., Snyder, D. A. & Rivers, M. L. (1992). An improved interference correction for trace element analysis. *Proceedings of the Annual Meeting-Electron Microscopy Society of America*: San francisco press, 1646-1646.

Donovan, J. J. & Tingle, T. N. (1996). An improved mean atomic number background correction for quantitative microanalysis. *Microscopy and Microanalysis* **2**, 1-7.

Fisher, G. W. (1970). The application of ionic equilibria to metamorphic differentiation: an example. *Contributions to Mineralogy and Petrology* **29**, 91-103.

Glodny, J., Kühn, A. & Austrheim, H. (2002). Rb/Sr record of fluid-rock interaction in eclogites, Bergen Arcs, Norway. *Geochimica et cosmochimica acta* **66**, A280-A280.

Glodny, J., Kühn, A. & Austrheim, H. (2008). Geochronology of fluid-induced eclogite and amphibolite facies metamorphic reactions in a subduction–collision system, Bergen Arcs, Norway. *Contributions to Mineralogy and Petrology* **156**, 27-48.

Grant, J. A. (1986). The isocon diagram; a simple solution to Gresens' equation for metasomatic alteration. *Economic geology* **81**, 1976-1982.

Green, E., White, R., Diener, J., Powell, R., Holland, T. & Palin, R. (2016). Activity–composition relations for the calculation of partial melting equilibria in metabasic rocks. *Journal of Metamorphic Geology* **34**, 845-869.

Hawthorne, F. C., Oberti, R., Harlow, G. E., Maresch, W. V., Martin, R. F., Schumacher, J. C. & Welch, M. D. (2012). Nomenclature of the amphibole supergroup. *American mineralogist* **97**, 2031-2048.

Hill, D. P. (2015). On the sensitivity of transtensional versus transpressional tectonic regimes to remote dynamic triggering by Coulomb failure. *Bulletin of the Seismological Society of America* **105**, 1339-1348.

Holland, T. & Powell, R. (2003). Activity–composition relations for phases in petrological calculations: an asymmetric multicomponent formulation. *Contributions to Mineralogy and Petrology* **145**, 492-501.

Holland, T. & Powell, R. (2011). An improved and extended internally consistent thermodynamic dataset for phases of petrological interest, involving a new equation of state for solids. *Journal of Metamorphic Geology* **29**, 333-383.

Joesten, R. (1977). Evolution of mineral assemblage zoning in diffusion metasomatism. *Geochimica et cosmochimica acta* **41**, 649-670.

Kelka, U., Veveakis, M., Koehn, D. & Beaudoin, N. (2017). Zebra rocks: compaction waves create ore deposits. *Scientific Reports* **7**, 1-9.

Koehn, D., Arnold, J., Jamtveit, B. & Malthe-Sørenssen, A. (2003). Instabilities in stress corrosion and the transition to brittle failure. *American Journal of Science* **303**, 956-971.

Kullerud, K. (1996). Chlorine-rich amphiboles; interplay between amphibole composition and an evolving fluid. *European Journal of Mineralogy* **8**, 355-370.

Lamadrid, H. M., Rimstidt, J. D., Schwarzenbach, E. M., Klein, F., Ulrich, S., Dolocan, A. & Bodnar, R. J. (2017). Effect of water activity on rates of serpentinization of olivine. *Nature communications* **8**, 16107.

Locock, A. J. (2014). An Excel spreadsheet to classify chemical analyses of amphiboles following the IMA 2012 recommendations. *Computers & Geosciences* **62**, 1-11.

Markl, G. & Bucher, K. (1998). Composition of fluids in the lower crust inferred from metamorphic salt in lower crustal rocks. *Nature* **391**, 781-783.

Markl, G., Ferry, J. & Bucher, K. (1998). Formation of saline brines and salt in the lower crust by hydration reactions in partially retrogressed granulites from the Lofoten Islands, Norway. *American Journal of Science* **298**, 705-757.

McDonough, W. F. & Sun, S.-S. (1995). The composition of the Earth. *Chemical geology* **120**, 223-253.

Moore, J., Beinlich, A., Porter, J. K., Talavera, C., Berndt, J., Piazolo, S., Austrheim, H. & Putnis, A. (2020). Microstructurally controlled trace element (Zr, U–Pb) concentrations in metamorphic rutile: An example from the amphibolites of the Bergen Arcs. *Journal of Metamorphic Geology* **38**, 103-127.

Moore, J., Beinlich, A., Putnis, A. & Austrheim, H. (2019). Stress orientation–dependent reactions during metamorphism. *Geology* **47**, 151-154.

Oelkers, E. H. & Helgeson, H. C. (1988). Calculation of the thermodynamic and transport properties of aqueous species at high pressures and temperatures: Aqueous tracer diffusion coefficients of ions to 1000°C and 5 kb. *Geochimica et cosmochimica acta* **52**, 63-85.

Orville, P. M. (1969). A model for metamorphic differentiation origin of thin-layered amphibolites. *American Journal of Science* **267**, 64-86.

Paterson, M. (1973). Nonhydrostatic thermodynamics and its geologic applications. *Reviews of Geophysics* **11**, 355-389.

Pattison, D. R. M. (1994). Are reversed Fe-Mg exchange and solid solution experiments really reversed? *American mineralogist* **79**, 938-950.

Porter, J. K. & Austrheim, H. (2017). Sulphide formation from granulite-facies S-rich scapolite breakdown. *Terra Nova* **29**, 29-35.

Powell, R. & Holland, T. (1988). An internally consistent dataset with uncertainties and correlations: 3. Applications to geobarometry, worked examples and a computer program. *Journal of Metamorphic Geology* **6**, 173-204.

Putnis, A. (2009). Mineral replacement reactions. *Reviews in mineralogy and geochemistry* **70**, 87-124.

Putnis, A. & Austrheim, H. (2013). Mechanisms of metasomatism and metamorphism on the local mineral scale: the role of dissolution-reprecipitation during mineral re-equilibration. *Metasomatism and the Chemical Transformation of Rock*: Springer, 141-170.

Rasband, W. S. (1997-2014). ImageJ. U. S. National Institutes of Health, Bethesda, MD. Available at http://imagej.nih.gov/ij/.

Rubie, D. C. (1986). The catalysis of mineral reactions by water and restrictions on the presence of aqueous fluid during metamorphism. *Mineralogical magazine* **50**, 399-415.

Rutter, E. (1983). Pressure solution in nature, theory and experiment. *Journal of the Geological Society* **140**, 725-740.

Selverstone, J., Morteani, G. & Staude, J. M. (1991). Fluid channelling during ductile shearing: transformation of granodiorite into aluminous schist in the Tauern Window, Eastern Alps. *Journal of Metamorphic Geology* **9**, 419-431.

Shimizu, I. (1995). Kinetics of pressure solution creep in quartz: theoretical considerations. *Tectonophysics* **245**, 121-134.

Shmulovich, K., Graham, C. & Yardley, B. (2001). Quartz, albite and diopside solubilities in H_2O–NaCl and H_2O–CO_2 fluids at 0.5–0.9 GPa. *Contributions to Mineralogy and Petrology* **141**, 95-108.

Vernon, R. (1979). Formation of late sillimanite by hydrogen metasomatism (base-leaching) in some high-grade gneisses. *Lithos* **12**, 143-152.

Vernon, R. (1998). Chemical and volume changes during deformation and prograde metamorphism of sediments. *Geological Society, London, Special Publications* **138**, 215-246.

Vernon, R. H. (2018). *A practical guide to rock microstructure*: Cambridge University Press.

Vidale, R. (1969). Metasomatism in a chemical gradient and the formation of calc-silicate bands. *American Journal of Science* **267**, 857-874.

Wassmann, S. & Stöckhert, B. (2013). Low stress deformation of garnet by incongruent dissolution precipitation creep. *Journal of Structural Geology* **46**, 200-219.

Wheeler, J. (2014). Dramatic effects of stress on metamorphic reactions. *Geology* **42**, 647-650.

Wheeler, J. (2018). The effects of stress on reactions in the Earth: Sometimes rather mean, usually normal, always important. *Journal of Metamorphic Geology* **36**, 439-461.

White, R., Powell, R., Holland, T., Johnson, T. & Green, E. (2014). New mineral activity–composition relations for thermodynamic calculations in metapelitic systems. *Journal of Metamorphic Geology* **32**, 261-286.

Whitney, D. L. & Evans, B. W. (2010). Abbreviations for names of rock-forming minerals. *American mineralogist* **95**, 185-187.

Williams, P. (1972). Development of metamorphic layering and cleavage in low grade metamorphic rocks at Bermagui, Australia. *American Journal of Science* **272**, 1-47.

Williams, P. F. (1990). Differentiated layering in metamorphic rocks. *Earth-Science Reviews* **29**, 267-281.

Wintsch, R. (1985). The possible effects of deformation on chemical processes in metamorphic fault zones. *Metamorphic reactions*: Springer, 251-268.

Wintsch, R., Kvale, C. & Kisch, H. (1991). Open-system, constant-volume development of slaty cleavage, and strain-induced replacement reactions in the Martinsburg Formation, Lehigh Gap, Pennsylvania. *Geological Society of America Bulletin* **103**, 916-927.

Wintsch, R. P. & Andrews, M. S. (1988). Deformation induced growth of sillimanite:" Stress" minerals revisited. *The Journal of Geology* **96**, 143-161.

Xia, F., Brugger, J., Chen, G., Ngothai, Y., O'Neill, B., Putnis, A. & Pring, A. (2009). Mechanism and kinetics of pseudomorphic mineral replacement reactions: A case study of the replacement of pentlandite by violarite. *Geochimica et cosmochimica acta* **73**, 1945-1969.

Yund, R. A. (1997). Rates of grain boundary diffusion through enstatite and forsterite reaction rims. *Contributions to Mineralogy and Petrology* **126**, 224-236.

FIGURE CAPTIONS

Figure 1. Regional setting and outcrop. (a) Study area at Radøy in the Lindås nappe of the Bergen Arcs, Western Norway. Outcrop locality is indicated by yellow star. Locality of amphibolite-facies shear zone of [1]Andersen *et al.* (1991) is indicated by white circle and scapolite veins of [2]Porter and Austrheim (2017) are indicated by red circles. MCTZ = Main Caledonian Thrust Zone. BASZ = Bergen Arcs Shear Zone. Modified from Boundy *et al.* (1997), Glodny *et al.* (2008) and Centrella *et al.* (2015). (b) Field relationships between lithologies at

Fjellsende (c) granulite to statically hydrated amphibolite interface, the continuation of the granulite foliation into the amphibolite is indicated by the dashed line (S). (d) Fracture and alteration halo in granulite. (e) Shear zone lithology showing a spaced foliation defined by interlayering of amphibolite and leucocratic domains.

Figure 2. TIMA-X Mineral maps for all lithologies: (a) Granulite, (b) fracture in granulite with detail of fracture assemblage inset (i). (c) Altered granulite, (d) Amphibolite (e) strained amphibolite exhibiting a quartz domain and four additional mineralogical domains (i-iv; for details see text), and the shear zone lithologies: (f) amphibolite domain (g) leucocratic domain exhibiting quartz stringers (i) with rare amphibole (ii), and, (h) quartz-enriched domain within a leucocratic domain.

Figure 3. Modal abundance of minerals in the separate lithologies across the granulite-shear zone interface. For each of the lithologies modal abundances are calculated as mass percentages based on representative TIMA-X maps. Spacing along the x-axis is representative of the distribution of the lithologies across the outcrop. Mineral abbreviations follow Whitney and Evans 2010.

Figure 4. Backscattered electron (BSE) images of representative assemblages at the granulite-amphibolite interface (a, b) and the replacement and breakdown of amphibole in the shear zone lithologies (c, d). (a, b) Grain boundary replacement of granulitic diopside, garnet, and plagioclase at by amphibolite assemblage. (c) Near-complete replacement of granulite-facies minerals in amphibolite. Replacement resulting in amphibolite-facies mineral distributions that are reflective of the precursor mineral. (d) Amphibole cluster in the shear zone amphibolite. (e) Elongate amphibole in the leucocratic domains.

Figure 5. BSE images (a, c-e) and photomicrograph of quartz-lined fractures and a quartz-enriched areas hosted in the main lithologies. (a) A quartz-lined fracture intersecting plagioclase

in the granulite. The fracture itself predominantly hosts quartz, oligoclase, bytownite and biotite. The alteration halo is comprised of large subhedral-euhedral zoisite, bytownite, andesine, quartz and minor amounts of kyanite and muscovite. (b) Microstructure of quartz aggregates within fracture (c) Quartz-filled fracture intersecting plagioclase in an altered granulite. Here the quartz on the fracture plane is accompanied by C-bearing scapolite and tschermakite (d) Foliation parallel quartz-enriched area in the strained amphibolite, comprised of quartz, muscovite, biotite and andesine. In the rock immediately adjacent to the fracture the size and abundance of zoisite and clinozoisite is increased, as reflected in the modal abundance of the rock (Fig. 3.3). (e) Quartz-enriched area within a leucocratic domain.

Figure 6. Amphibole compositions across the granulite-shear zone transition. All amphiboles belong to the amphibolite alteration event. (a) Ca-amphibole classification plot with Cl apfu contouring. (b) X_{Mg} versus Cl apfu with the range of concentrations indicated for each of the lithologies.

Figure 7. Scapolite composition (a) S apfu and (b) Cl apfu in scapolite A-site plotted against equivalent anorthite component. (c) Photomicrograph of S-bearing scapolite vein in an altered granulite. BSE images of: (d) recrystallisation at S-bearing scapolite grain boundaries, producing S-poor scapolite and pyrite. (e) C-rich scapolite aggregate in the amphibolite (f) scapolite in the amphibolite domains of the shear zone.

Figure 8. Bulk chemistry mass change of major and volatile elements (wt%) in the amphibolite-facies lithologies relative to the anorthositic granulite. In all lithologies plagioclase forming elements (SiO_2, Al_2O_3, Na_2O, and CaO) are highlighted.

Figure 9. Comparison granulite and amphibolite-facies whole rock REE patterns.

Figure 10. Thermodynamic modelling of amphibolite mineral assemblages in (a-c) T–X_{H2O} and (d) P–T pseudosections. For each of the T–X_{H2O} pseudosections zoisite modal isopleths are indicated within the assemblage stability fields. (a) The amphibolite mineral assemblage, with zoisite at 3 modal %, is stable when bulk H_2O content is increased from the measured amount (X_0: 0.26 wt%) to 0.77-0.85 wt%. (b) The amphibolite domain mineral assemblage, with zoisite at 3 modal %, is stable when bulk H_2O content is increased from the measured amount (X_0: 0.36 wt%) to 0.95-1.10 wt%. (b) The leucocratic domain mineral assemblage, with zoisite at 6 modal %, is stable at the measured H_2O content (X_0: 0.48 wt%). (d) Amphibolite, amphibolite domain and leucocratic domain assemblages modelled in P–T space with the equilibrium H_2O content as indicated by T–X_{H2O} diagrams. Mineral stability fields (i, ii) for the amphibolite assemblages and (iii) for the leucocratic domains, are consistent with the results of individual geothermobarometers (for details see; Moore *et al.*, 2020).

Figure 11. Thermodynamic modelling of mass transfer and assemblage distribution in the shear zone rock. (a) P–X pseudosection of the shear zone rock lithologies at the thermodynamically estimated H_2O composition. Beneath the pseudosection is the mass change comparison of the leucocratic domains and amphibolite domains within the shear zone rock and the entire shear zone rock in comparison to the granulite. (b) Calculated mineral mass percentages at the observed zoisite abundances each composition. (c) Observed mineral mass percentages in the shear zone lithologies.

Figure 12. Comparison of the calculated partial melt mass changes (a, b) with the measured mass change in the shear zone lithologies (c, d). All mass gains and losses are relative to the anhydrous granulite.

Figure 13. Conceptual model for the characteristic elemental and textural distributions associated with the amphibolite facies hydration and deformation event. (a) Initial fluid infiltrates granulite along pre-existing fractures of varying size. Fractures are illustrated as concentrated damage zones, the damage to the rock progressively decreasing outwards from the central fracture, providing pathways for the percolation of fluid outwards from fractures. The stages illustrated in (b) and (c) are simultaneous. (b) Illustration of the initial stress distribution that results from the fracturing. The concentration of stress on a central plane enhances both fluid availability and dissolution within that zone (c) Due to the heterogeneous strain and fluid distribution the minerals grown in each domain have different characteristic textures. Minerals grown in the central fracture - quartz-enriched domains- have a microstructure characteristic of crystal growth in a free fluid. Minerals grown in the outer fracture damage zones - the amphibolite - are characteristic of interface-coupled dissolution and precipitation, leading to pseudomorphic replacement of granulite facies minerals. In areas where fracture zones are relatively small (I) then deformation is not induced and fluid connectivity is reduced, resulting in continued reaction within a system that is closed at the mm to cm scale, as shown in (d). Here H_2O consuming reactions leave a final fluid that is concentrated in Cl, precipitating Cl-enriched minerals along fractures. In areas where fracture damage zones are sufficiently large (II) and the localisation of shear is facilitated as shown in (e) then deformation enables continued fluid connectivity on at least the cm-dm scale. The combined continued fluid connectivity and deformation results in a system that is open at this larger scale. Continued connectivity results in the leaching of elements (Mg, Fe, and K) from the leucocratic domains, transporting them into the amphibolite domains.

Figure 1

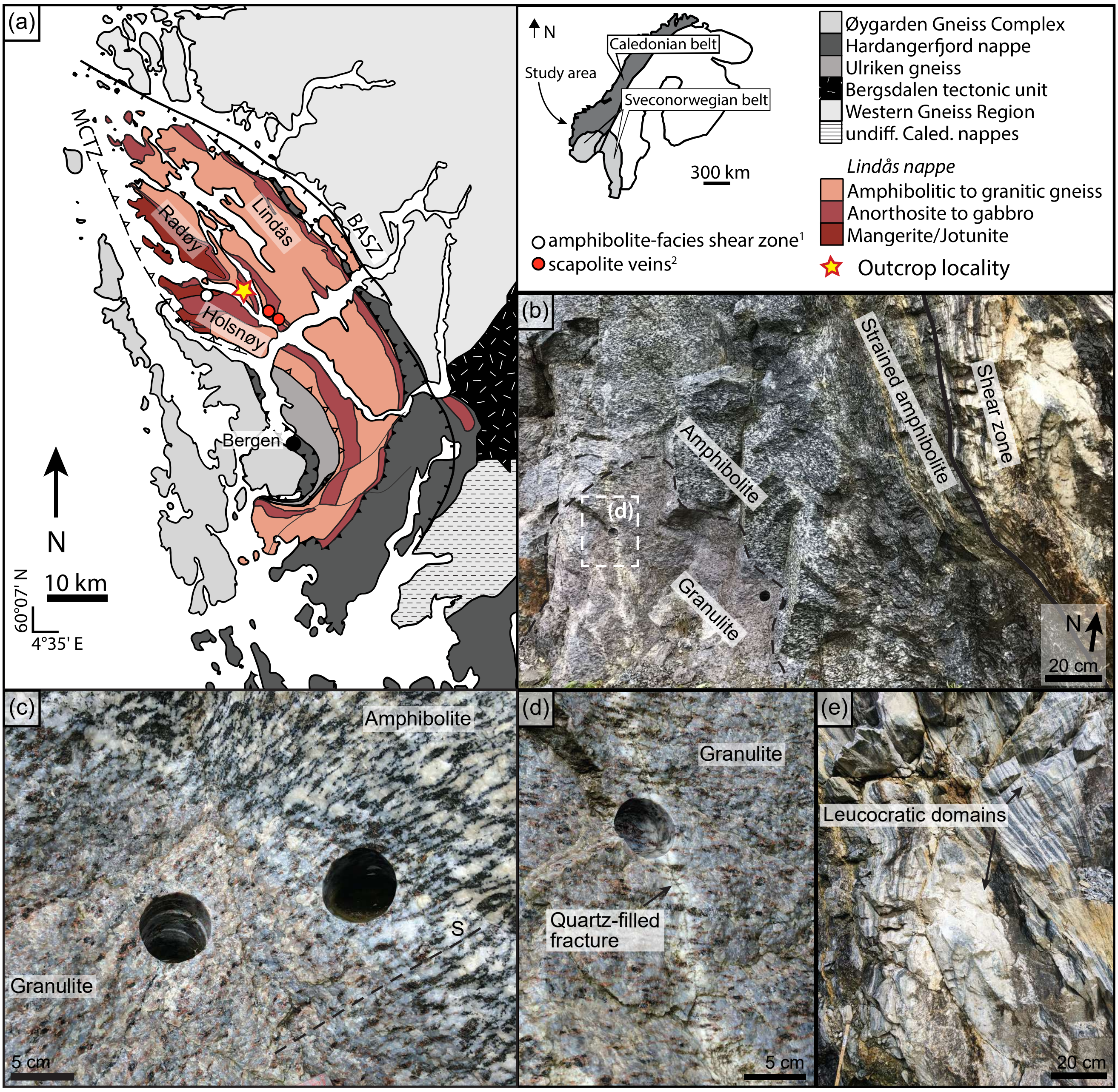
(a)
MCTZ
Radøy
Lindås
BASZ
Holsnøy
Bergen
N
10 km
60°07' N
4°35' E
N
Caledonian belt
Study area
Sveconorwegian belt
300 km
○ amphibolite-facies shear zone[1]
● scapolite veins[2]
Øygarden Gneiss Complex
Hardangerfjord nappe
Ulriken gneiss
Bergsdalen tectonic unit
Western Gneiss Region
undiff. Caled. nappes
Lindås nappe
Amphibolitic to granitic gneiss
Anorthosite to gabbro
Mangerite/Jotunite
☆ Outcrop locality
(b)
Strained amphibolite
Shear zone
Amphibolite
(d)
Granulite
N
20 cm
(c)
Amphibolite
S
Granulite
5 cm
(d)
Granulite
Quartz-filled fracture
5 cm
(e)
Leucocratic domains
20 cm

Figure 2

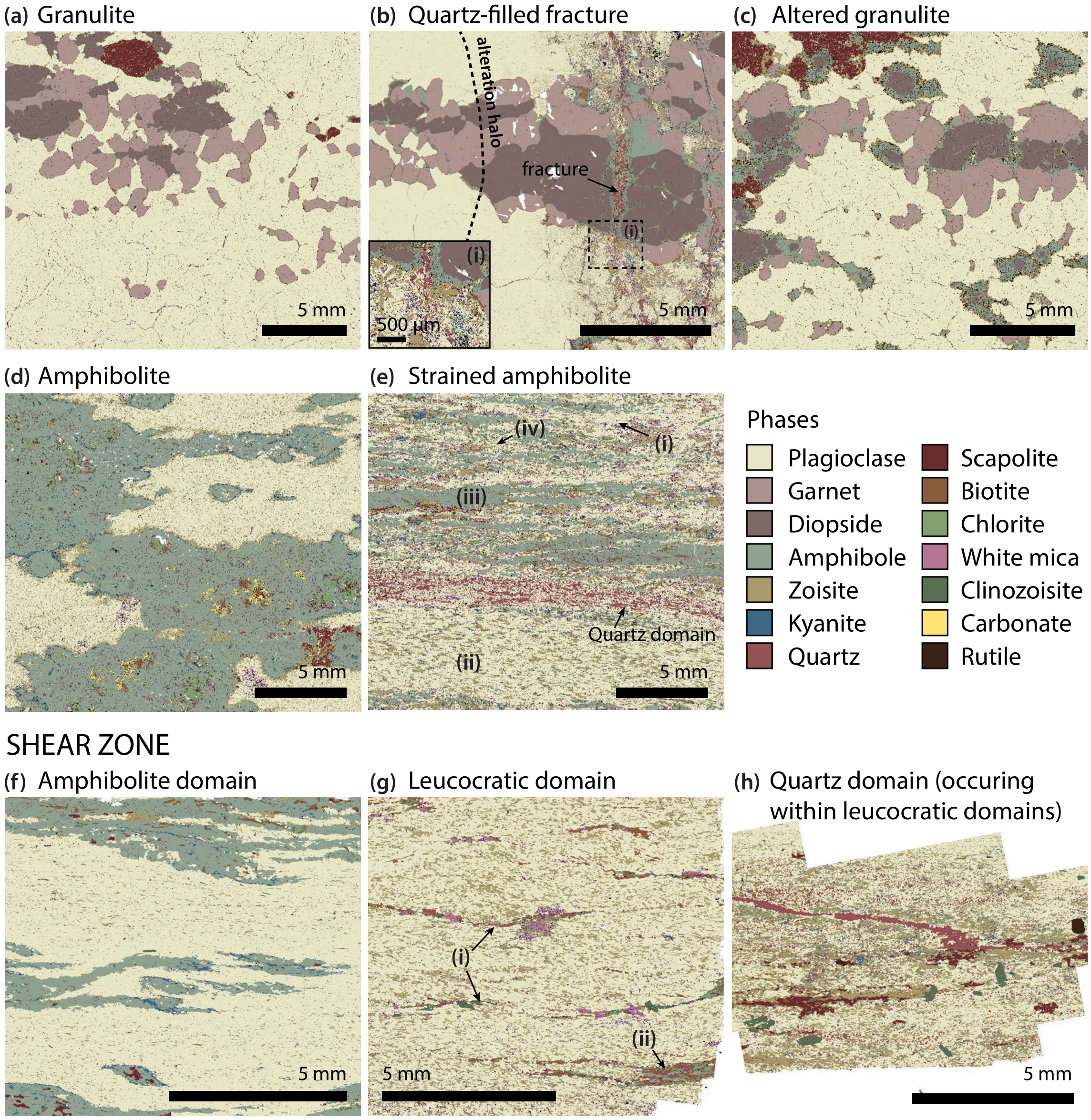
(a) Granulite
5 mm
(b) Quartz-filled fracture
alteration halo
fracture
(i)
500 µm
5 mm
(c) Altered granulite
5 mm
(d) Amphibolite
5 mm
(e) Strained amphibolite
(iv)
(i)
(iii)
Quartz domain
(ii)
5 mm
Phases
Plagioclase
Garnet
Diopside
Amphibole
Zoisite
Kyanite
Quartz
Scapolite
Biotite
Chlorite
White mica
Clinozoisite
Carbonate
Rutile
SHEAR ZONE
(f) Amphibolite domain
5 mm
(g) Leucocratic domain
(i)
(ii)
5 mm
(h) Quartz domain (occuring within leucocratic domains)
5 mm

Figure 3

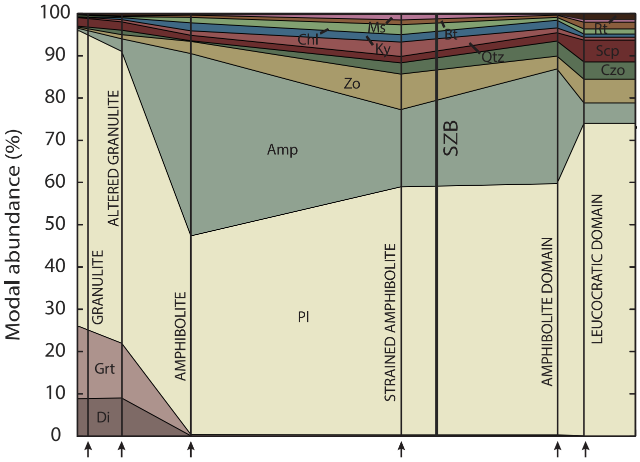
100
90
80
70
60
50
40
30
20
10
0
Modal abundance (%)
GRANULITE
ALTERED GRANULITE
AMPHIBOLITE
STRAINED AMPHIBOLITE
SZB
AMPHIBOLITE DOMAIN
LEUCOCRATIC DOMAIN
Chl
Ms
Ky
Bt
Qtz
Rt
Scp
Czo
Zo
Amp
Pl
Grt
Di

Figure 4

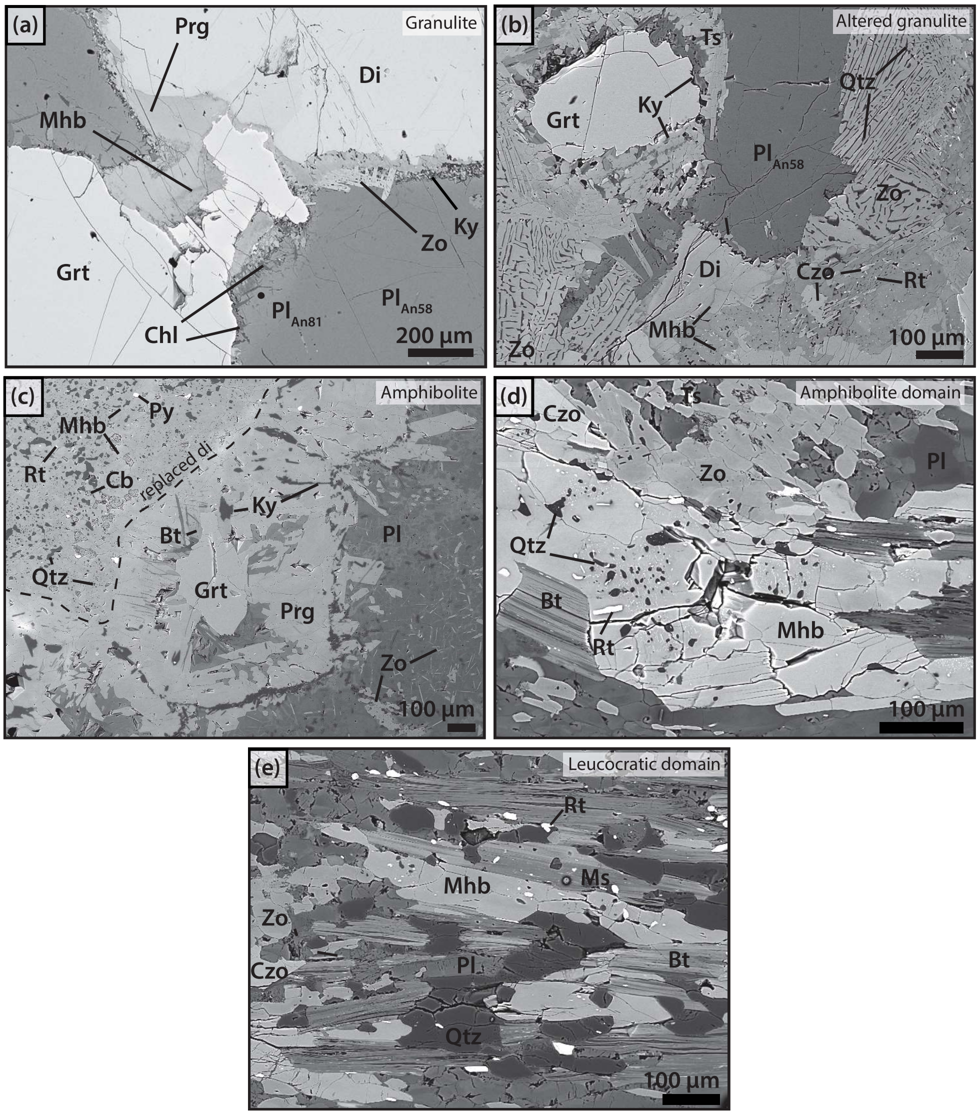
(a)
Granulite
Prg
Di
Mhb
Zo
Ky
Grt
Chl
Pl$_{An81}$
Pl$_{An58}$
200 µm
(b)
Altered granulite
Ts
Qtz
Grt
Ky
Pl$_{An58}$
Zo
Di
Czo
Rt
Mhb
Zo
100 µm
(c)
Amphibolite
Py
Mhb
Rt
Cb
replaced di
Ky
Bt
Pl
Qtz
Grt
Prg
Zo
100 µm
(d)
Amphibolite domain
Czo
Ts
Zo
Pl
Qtz
Bt
Rt
Mhb
100 µm
(e)
Leucocratic domain
Rt
Mhb
Ms
Zo
Czo
Pl
Bt
Qtz
100 µm

Figure 5

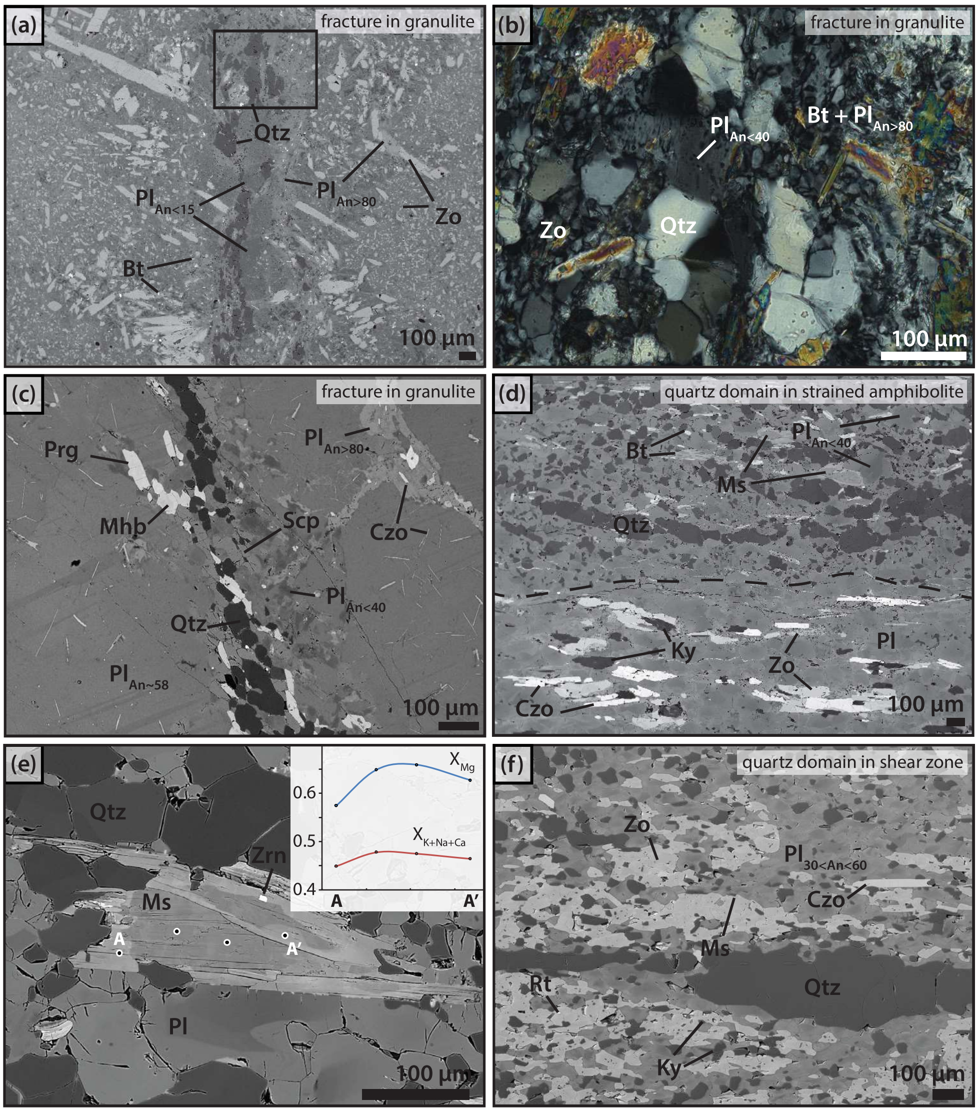
(a)
fracture in granulite
Qtz
Pl$_{An<15}$
Pl$_{An>80}$
Zo
Bt
100 µm
(b)
fracture in granulite
Pl$_{An<40}$
Bt + Pl$_{An>80}$
Zo
Qtz
100 µm
(c)
fracture in granulite
Prg
Pl$_{An>80}$
Mhb
Scp
Czo
Pl$_{An<40}$
Qtz
Pl$_{An\sim58}$
100 µm
(d)
quartz domain in strained amphibolite
Bt
Pl$_{An<40}$
Ms
Qtz
Ky
Zo
Pl
Czo
100 µm
(e)
Qtz
Zrn
Ms
A
A'
Pl
100 µm
X$_{Mg}$
X$_{K+Na+Ca}$
0.6
0.5
0.4
A
A'
(f)
quartz domain in shear zone
Zo
Pl$_{30<An<60}$
Czo
Ms
Rt
Qtz
Ky
100 µm

Figure 6

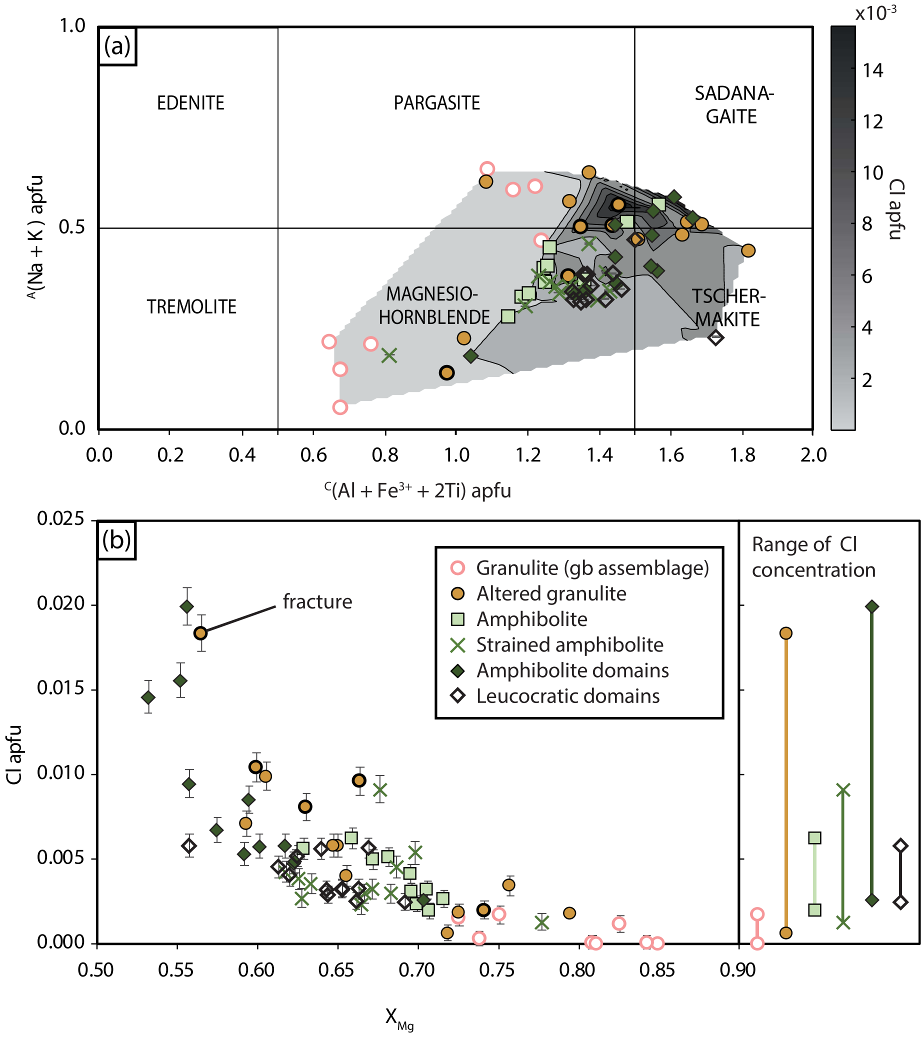
(a)
EDENITE
PARGASITE
SADANA-GAITE
TREMOLITE
MAGNESIO-HORNBLENDE
TSCHER-MAKITE
^A(Na + K) apfu
1.0
0.5
0.0
0.0
0.2
0.4
0.6
0.8
1.0
1.2
1.4
1.6
1.8
2.0
^C(Al + Fe^3+ + 2Ti) apfu
x10^-3
14
12
10
8
6
4
2
Cl apfu
(b)
fracture
Granulite (gb assemblage)
Altered granulite
Amphibolite
Strained amphibolite
Amphibolite domains
Leucocratic domains
Range of Cl concentration
Cl apfu
0.025
0.020
0.015
0.010
0.005
0.000
0.50
0.55
0.60
0.65
0.70
0.75
0.80
0.85
0.90
X_Mg

Figure 7

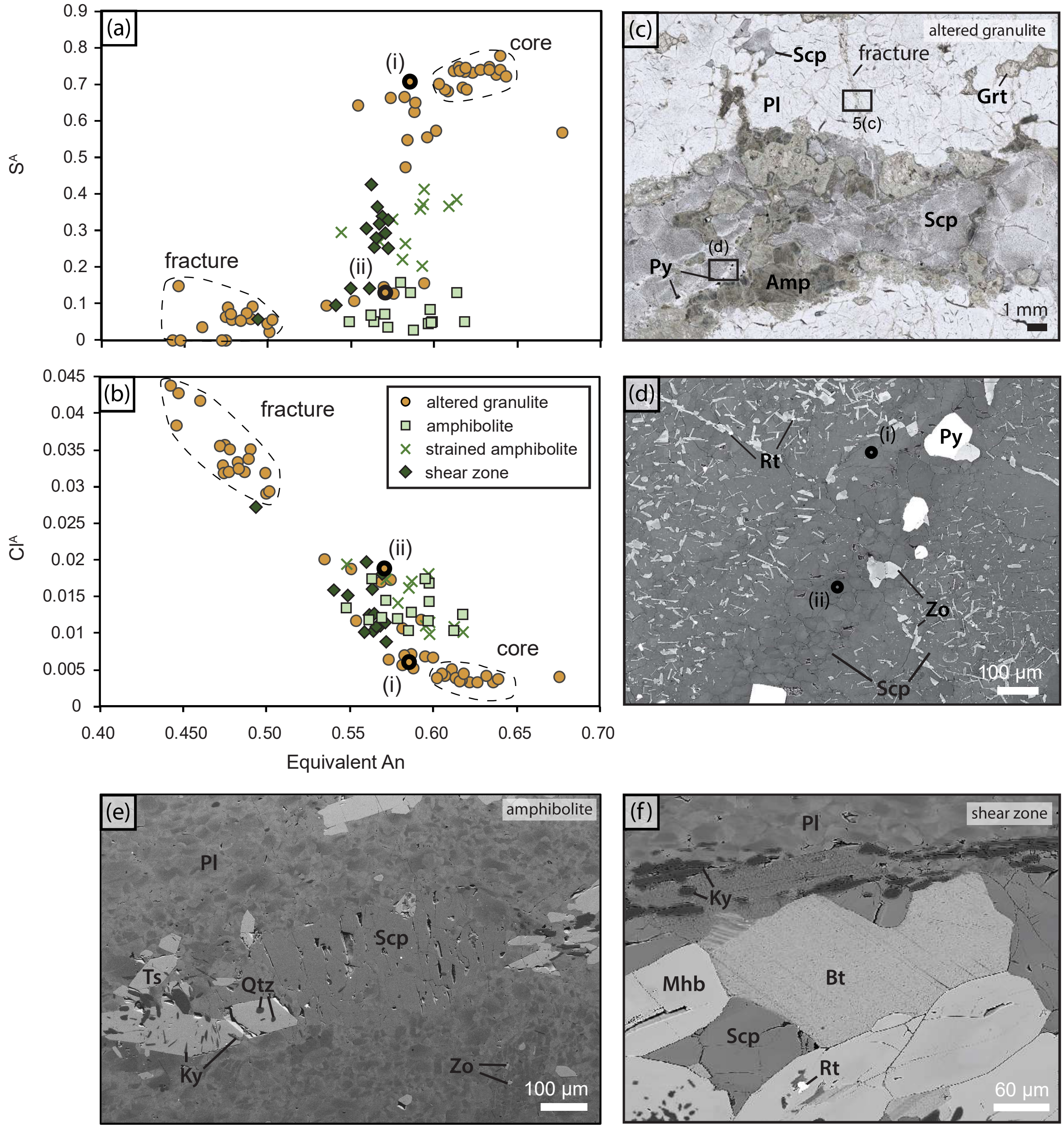
(a)
core
(i)
(ii)
fracture
S^A
0.9
0.8
0.7
0.6
0.5
0.4
0.3
0.2
0.1
0
(b)
fracture
altered granulite
amphibolite
strained amphibolite
shear zone
Cl^A
0.045
0.04
0.035
0.03
0.025
0.02
0.015
0.01
0.005
0
(ii)
core
(i)
0.40
0.450
0.50
0.55
0.60
0.65
0.70
Equivalent An
(c)
altered granulite
Scp
fracture
Pl
5(c)
Grt
Scp
(d)
Py
Amp
1 mm
(d)
Rt
(i)
Py
(ii)
Zo
Scp
100 µm
(e)
amphibolite
Pl
Scp
Ts
Qtz
Ky
Zo
100 µm
(f)
shear zone
Pl
Ky
Mhb
Bt
Scp
Rt
60 µm

Figure 8

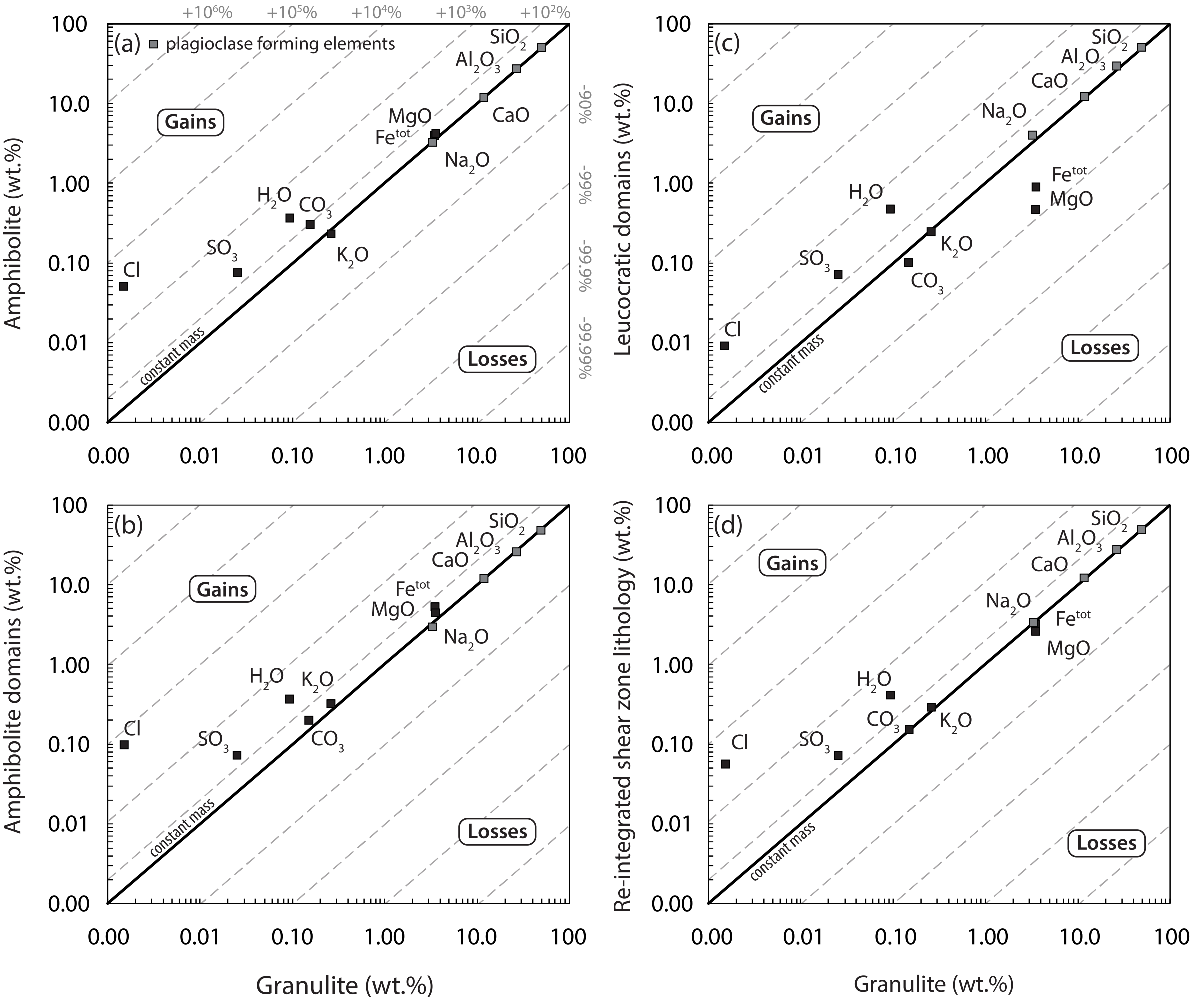
(a)
plagioclase forming elements
+10⁶%
+10⁵%
+10⁴%
+10³%
+10²%
-90%
-99%
-99.9%
-99.99%
Gains
Losses
constant mass
SiO2
Al2O3
CaO
MgO
Fetot
Na2O
H2O
CO3
K2O
SO3
Cl
Amphibolite (wt.%)
(b)
Amphibolite domains (wt.%)
(c)
Leucocratic domains (wt.%)
(d)
Re-integrated shear zone lithology (wt.%)
Granulite (wt.%)
100
10.0
1.00
0.10
0.01
0.00

Figure 9

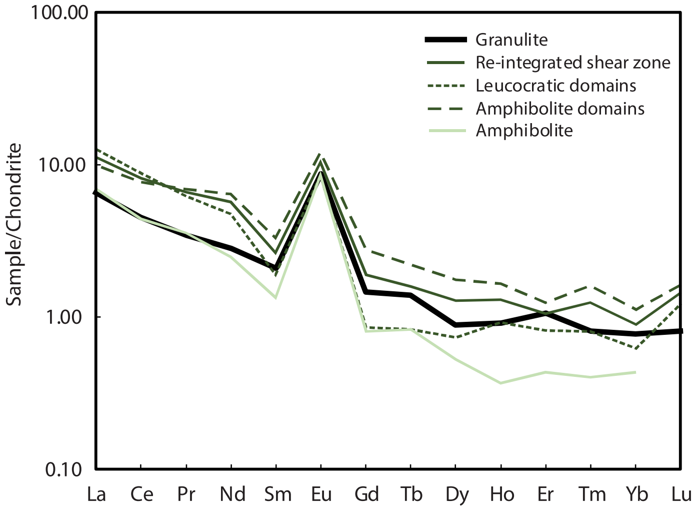
100.00
10.00
1.00
0.10
Sample/Chondrite
La
Ce
Pr
Nd
Sm
Eu
Gd
Tb
Dy
Ho
Er
Tm
Yb
Lu
Granulite
Re-integrated shear zone
Leucocratic domains
Amphibolite domains
Amphibolite

Figure 10

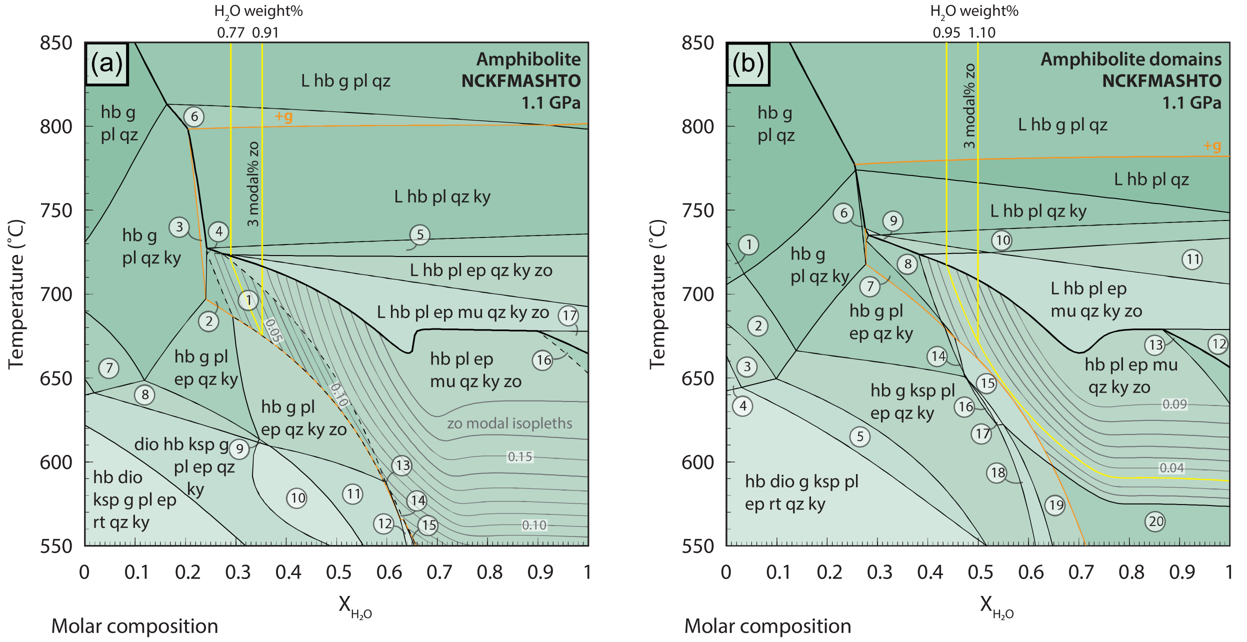

Molar composition

	SiO$_2$	TiO$_2$	Al$_2$O$_3$	FeO	MgO	CaO	Na$_2$O	K$_2$O	O$_2$	H$_2$O
X$_0$	54.2	0.08	17.2	2.49	6.72	13.6	3.43	0.16	0.27	1.30
X$_1$	51.6	0.08	16.3	2.38	6.40	12.9	3.27	0.15	0.26	6.20

1. hb pl ep qz ky zo
2. hb pl ep qz ky
3. hb pl qz ky
4. hb pl qz ky zo
5. L hb pl qz ky zo
6. L hb g pl qz ky
7. dio hb g pl qz ky
8. dio hb g pl ep qz ky
9. dio hb g pl ep qz ky zo
10. dio hb ksp g pl ep qz ky zo
11. hb ksp g pl ep qz ky zo
12. hb ksp g pl ep mu qz ky zo
13. hb ksp pl ep qz ky zo
14. hb ksp pl ep mu qz ky zo
15. hb g pl ep mu qz ky zo
16. hb pl ep mu qz zo
17. L hb pl ep mu qz zo

Molar composition

	SiO$_2$	TiO$_2$	Al$_2$O$_3$	FeO	MgO	CaO	Na$_2$O	K$_2$O	O$_2$	H$_2$O
X$_0$	52.6	0.13	16.7	3.33	7.13	13.7	3.13	0.22	0.38	1.31
X$_1$	50.3	0.13	15.9	3.19	6.83	13.1	3.00	0.21	0.36	6.56

1. hb g ksp pl qz
2. hb g ksp pl qz ky
3. dio hb g ksp pl qz ky
4. dio hb g ksp pl rt qz ky
5. dio hb g ksp pl ep qz ky
6. hb g pl qz
7. hb pl ep qz ky
8. hb pl ep mu qz ky
9. L hb pl ep mu qz ky
10. L hb pl ep qz ky
11. L hb pl ep qz ky zo
12. L hb pl ep qz zo
13. hb pl ep qz zo
14. hb g pl ep qz ky zo
15. hb g pl ep mu qz ky zo
16. hb g ksp pl ep qz ky zo
17. hb g ksp pl ep mu qz ky zo
18. hb g ksp pl ep mu qz ky
19. hb g pl ep mu qz ky
20. hb pl ep mu qz ky

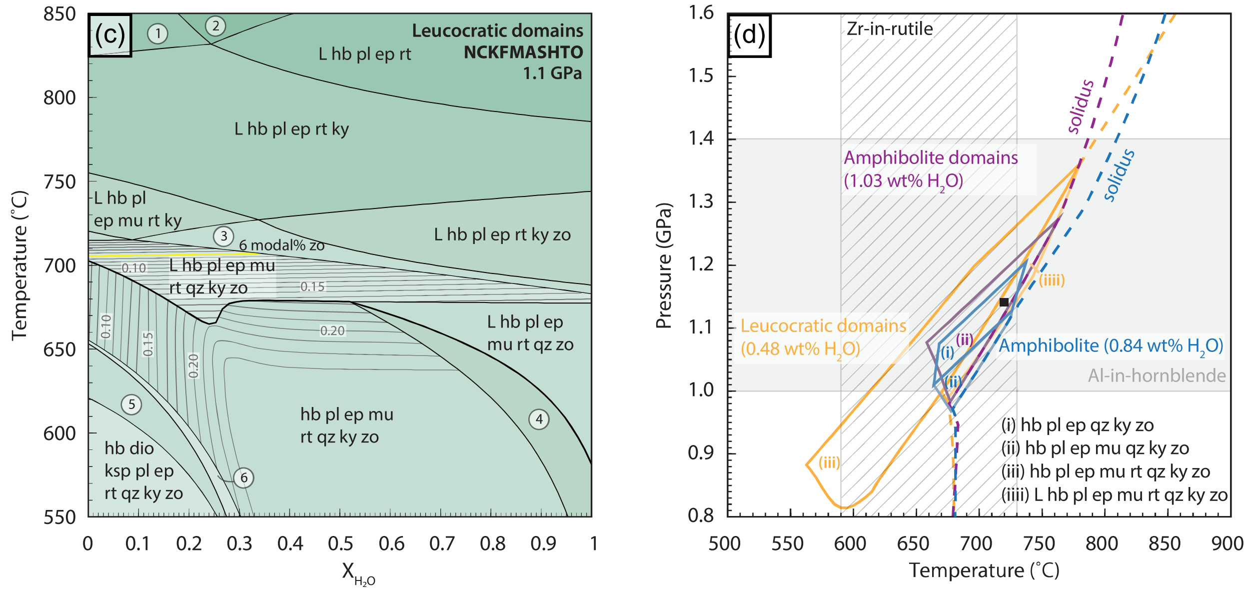

Molar composition

	SiO$_2$	TiO$_2$	Al$_2$O$_3$	FeO	MgO	CaO	Na$_2$O	K$_2$O	O$_2$	H$_2$O
X$_0$	57.6	0.07	19.7	0.29	0.77	15.1	4.38	0.18	0.14	1.77
X$_1$	54.5	0.06	18.7	0.28	0.73	14.3	4.14	0.17	0.13	7.10

1. L hb pl rt ky
2. L hb pl ep rt
3. L hb pl ep mu rt ky zo
4. hb pl ep mu rt qz zo
5. hb ksp pl ep rt qz ky zo
6. hb ksp pl ep mu rt qz ky zo

■ 720˚C and 1.14 GPa
Amphibolite a_{H_2O} = 0.63
Amphibolite domains a_{H_2O} = 0.77
Leucocratic domains a_{H_2O} = 0.87

Figure 11

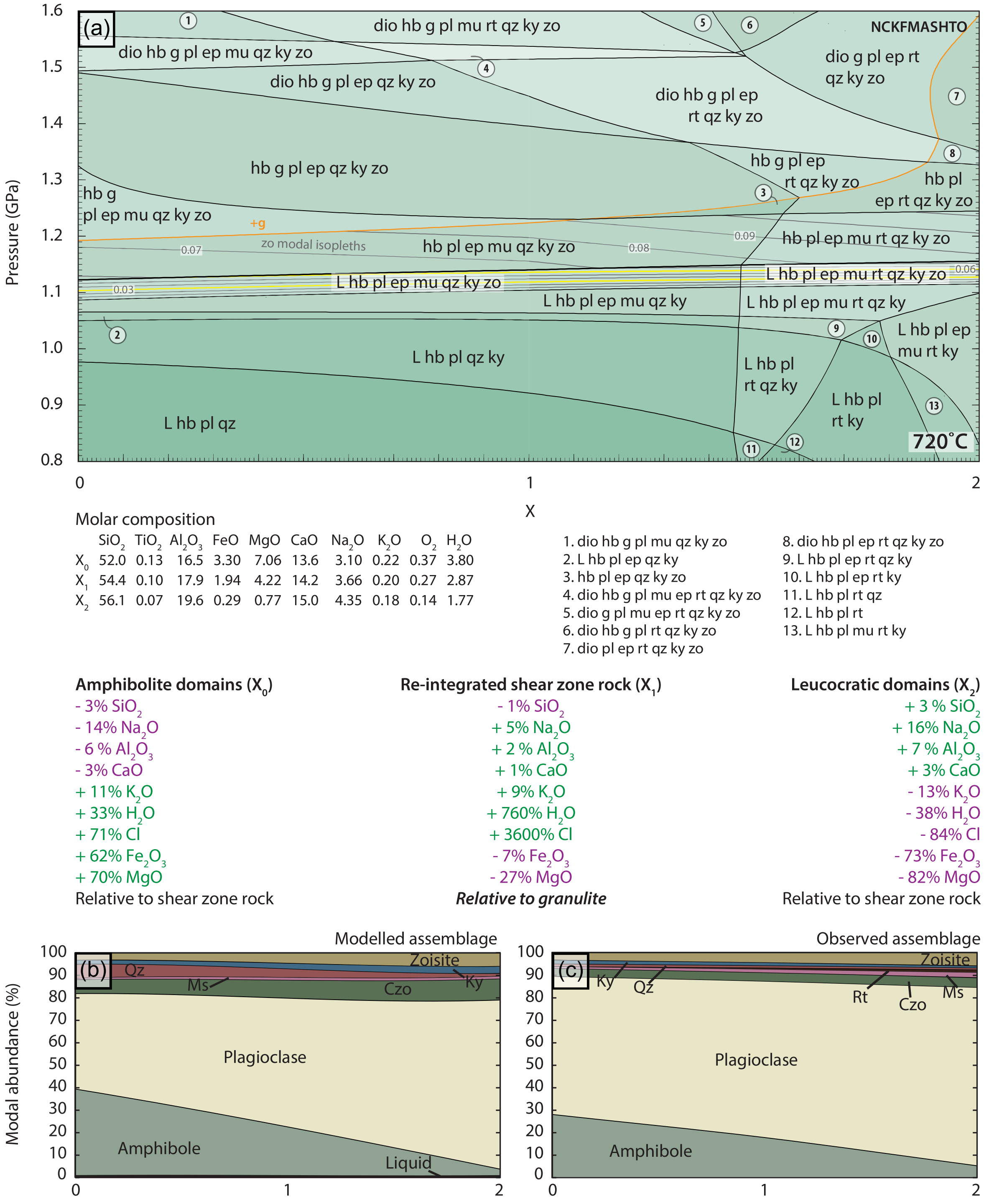

Molar composition

	SiO_2	TiO_2	Al_2O_3	FeO	MgO	CaO	Na_2O	K_2O	O_2	H_2O
X_0	52.0	0.13	16.5	3.30	7.06	13.6	3.10	0.22	0.37	3.80
X_1	54.4	0.10	17.9	1.94	4.22	14.2	3.66	0.20	0.27	2.87
X_2	56.1	0.07	19.6	0.29	0.77	15.0	4.35	0.18	0.14	1.77

1. dio hb g pl mu qz ky zo
2. L hb pl ep qz ky
3. hb pl ep qz ky zo
4. dio hb g pl mu ep rt qz ky zo
5. dio g pl mu ep rt qz ky zo
6. dio hb g pl rt qz ky zo
7. dio pl ep rt qz ky zo
8. dio hb pl ep rt qz ky zo
9. L hb pl ep rt qz ky
10. L hb pl ep rt ky
11. L hb pl rt qz
12. L hb pl rt
13. L hb pl mu rt ky

Amphibolite domains (X_0)	**Re-integrated shear zone rock (X_1)**	**Leucocratic domains (X_2)**
- 3% SiO_2	- 1% SiO_2	+ 3 % SiO_2
- 14% Na_2O	+ 5% Na_2O	+ 16% Na_2O
- 6 % Al_2O_3	+ 2 % Al_2O_3	+ 7 % Al_2O_3
- 3% CaO	+ 1% CaO	+ 3% CaO
+ 11% K_2O	+ 9% K_2O	- 13% K_2O
+ 33% H_2O	+ 760% H_2O	- 38% H_2O
+ 71% Cl	+ 3600% Cl	- 84% Cl
+ 62% Fe_2O_3	- 7% Fe_2O_3	- 73% Fe_2O_3
+ 70% MgO	- 27% MgO	- 82% MgO
Relative to shear zone rock	***Relative to granulite***	Relative to shear zone rock

Figure 12

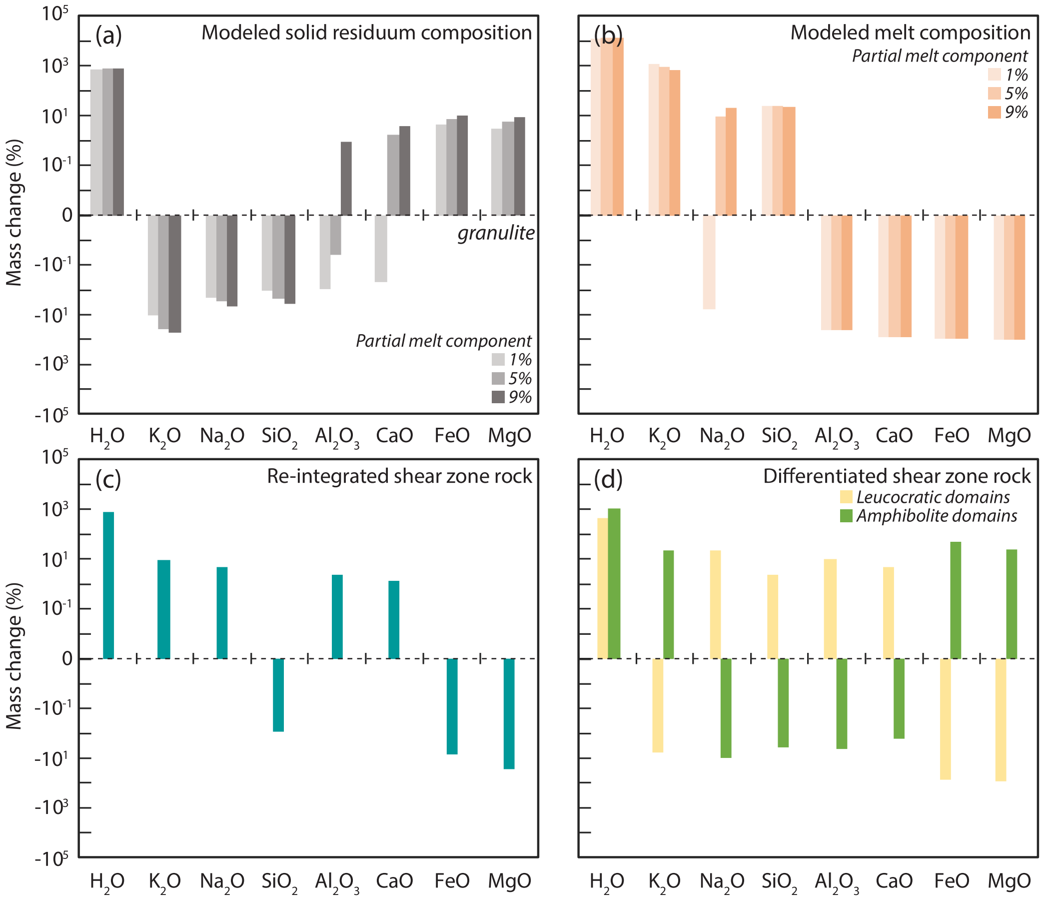
(a) Modeled solid residuum composition
Mass change (%)
granulite
Partial melt component
1%
5%
9%
(b) Modeled melt composition
Partial melt component
1%
5%
9%
(c) Re-integrated shear zone rock
(d) Differentiated shear zone rock
Leucocratic domains
Amphibolite domains
10^5
10^3
10^1
10^-1
0
-10^-1
-10^1
-10^3
-10^5
H2O
K2O
Na2O
SiO2
Al2O3
CaO
FeO
MgO

Figure 13

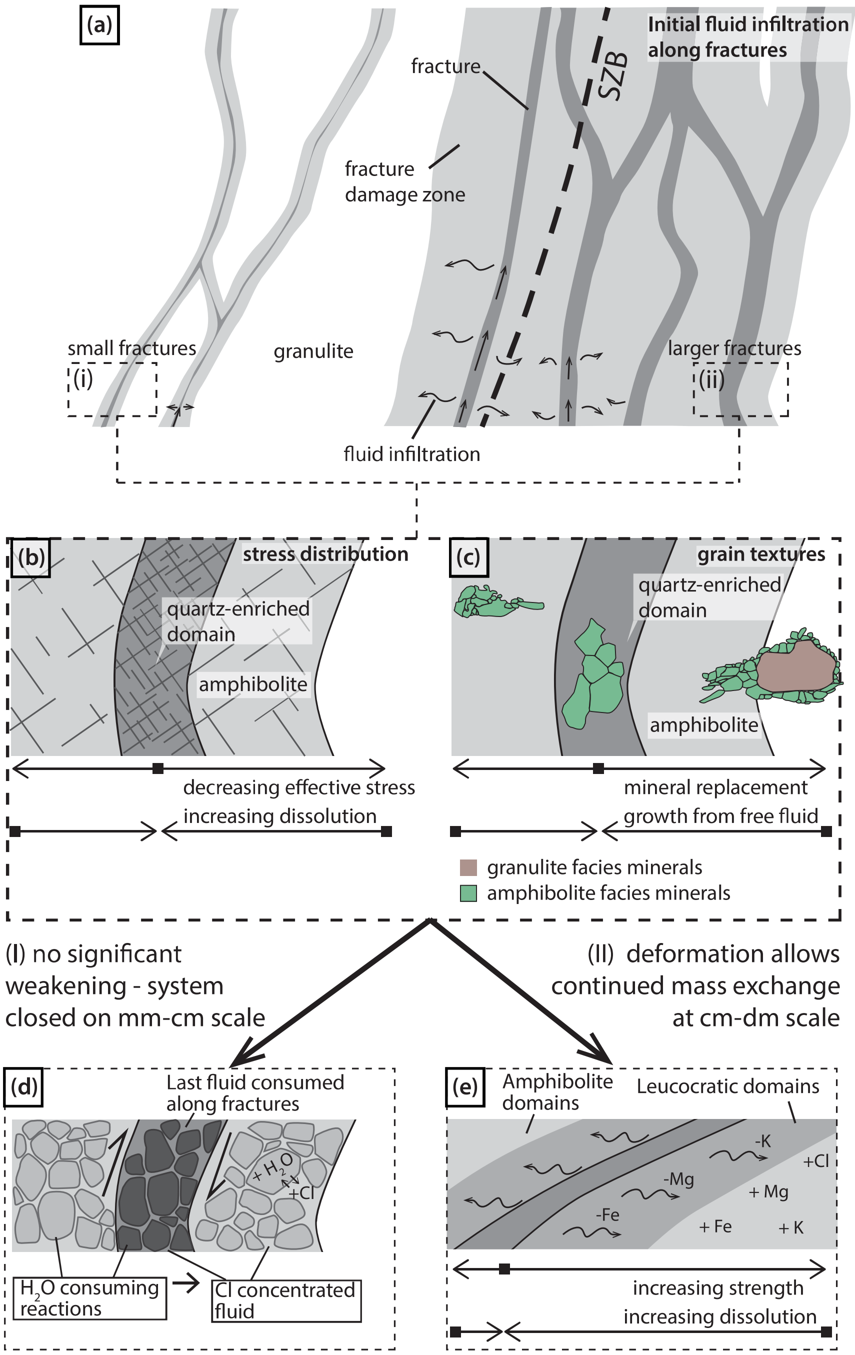
(a)
Initial fluid infiltration along fractures
fracture
SZB
fracture damage zone
small fractures
(i)
granulite
larger fractures
(ii)
fluid infiltration
(b)
stress distribution
quartz-enriched domain
amphibolite
decreasing effective stress
increasing dissolution
(c)
grain textures
quartz-enriched domain
amphibolite
mineral replacement
growth from free fluid
granulite facies minerals
amphibolite facies minerals
(I) no significant weakening - system closed on mm-cm scale
(II) deformation allows continued mass exchange at cm-dm scale
(d)
Last fluid consumed along fractures
+ H₂O
+Cl
H₂O consuming reactions
Cl concentrated fluid
(e)
Amphibolite domains
Leucocratic domains
-K
+Cl
-Mg
+ Mg
-Fe
+ Fe
+ K
increasing strength
increasing dissolution

Table 1. Representative Whole rock analyses of major elements (XRF).

Number of analyses (N)	2		2		3		1	1	
Density	2.87		2.86		2.83		2.89	2.80	
Sample	Granulite	SE	Amphibolite	SE	Strained amphibolite	SE	Shear zone amphibolite	Leucocratic domains	Re-integrated shear zone rock
SiO_2	50.1	0.18	49.4	0.020	50.1	0.21	48.3	51.3	49.7
Al_2O_3	27.1	0.065	26.6	0.080	26.2	0.26	26.0	29.8	27.7
Fe_2O_3	0.263	0.078	0.876	0.011	0.767	0.11	1.24	0.555	0.926
FeO	2.94	0.12	2.73	0.020	2.54	0.10	3.66	0.310	2.12
MnO	0.04		0.05		0.04		0.07	0.01	0.04
MgO	3.54	0.14	4.12	0.085	3.61	0.22	4.4	0.46	2.59
CaO	12.0	0.055	11.5	0.040	11.4	0.15	11.8	12.5	12.1
Na_2O	3.3	0.060	3.23	0.020	3.46	0.035	2.97	4.02	3.45
K_2O	0.262	0.0080	0.231	0.011	0.425	0.048	0.318	0.247	0.285
SO_3	0.0255	0.0045	0.0740	0.0060	0.0847	0.022	0.0720	0.0710	0.0715
CO_3	0.150		0.300		0.250		0.200	0.100	0.150
Cl	0.0015	0.00071	0.050	0.018	0.057	0.014	0.095	0.0090	0.057
H_2O (LOI)	0.095	0.14	0.36	0.10	0.61	0.17	0.36	0.48	0.41
Total	99.8		99.5		99.5		99.4	99.9	99.6
Fe^{tot}	3.53		3.91		3.59		5.31	0.900	3.28
H_2O (Thermocalc)	0.095		0.84				1.0	0.48	0.78